Cement and Concrete Research 174 (2023) 107324

Contents lists available at ScienceDirect

Cement and Concrete Research

journal homepage: www.elsevier.com/locate/cemconres

Organic cross-linking decreases the thermal conductivity of calcium silicate hydrates

Amir Moshiri [a,1,2], Ali Morshedifard [b,1], Damian Stefaniuk [a,3], Santiago El Awad [a], Tejasree Phatak [a], Kamil J. Krzywiński [c], Debora Frigi Rodrigues [a], Mohammad Javad Abdolhosseini Qomi [b,*], Konrad J. Krakowiak [a,*]

[a] Civil and Environmental Engineering Department, Cullen College of Engineering, University of Houston, Engineering Building 1, Room N-107, 4226 Martin Luther King Boulevard, Houston, TX 77204-4003, United States

[b] Advanced Infrastructure Materials for Sustainability Laboratory (AIMS Lab), Department of Civil and Environmental Engineering, Henry Samueli School of Engineering, E4130 Engineering Gateway, University of California, Irvine, CA 92697-2175, United States

[c] Faculty of Civil Engineering, Wroclaw University of Science and Technology, Wybrzeze Wyspianskiego 27, 50-370 Wroclaw, Poland

ARTICLE INFO

Keywords:
Calcium-silicate-hydrate
Organic molecules
Cross-linking
Thermal conductivity
Experiments and simulations

ABSTRACT

We study the conductive heat transport through calcium silicate hydrate (C-S-H) and organically cross-linked C-S-H via experiments, micromechanical homogenization theory, and molecular simulations. We find that C-S-H's intrinsic thermal conductivity falls below its amorphous limit when cross-linked with short-chain organosilanes. The observed reduction correlates with the alkyl chain length of the bis-organosilane molecule. To understand the underlying fundamental molecular processes accountable for such a reduction, we construct realistic molecular structures of cross-linked C-S-H and validate them against the spectroscopic and pycnometery measurements. The atomistic simulations indicate that the reduction in the contribution of propagons (propagating heat carriers) and diffusons (diffusive heat carriers) to heat transport, and the amplification of locons (localized vibrational modes), are the main driving factors allowing to limit the heat conduction in C-S-H. Presented findings offer new potential directions to nanoengineering novel admixtures for cement composites and resilient lightweight cementitious mesostructures for thermally efficient building envelopes.

1. Introduction

Despite high technological relevance, heat transport phenomena in the calcium-silicate-hydrate (C-S-H), the main constituent in hydrated colloidal cement systems [1], has not received commensurate attention until recently. Thanks to the rapid advancement in computational statistical mechanics [2–4], molecular dynamics (MD) simulations have become a powerful tool for estimating the intrinsic thermal conductivity tensor (λ) of C-S-H at the nanoscale in the absence of the relevant experimental data (e.g. its volumetric average $\lambda_v = (\lambda_{11} + \lambda_{22} + \lambda_{33})/3 \approx 1$ Wm^{-1} K^{-1} at 300 K, and the specific heat capacity, c_v). Apart from these fundamental estimates, molecular simulations also revealed a critical observation having far-reaching implications for the conductive heat transfer in cementitious materials. The λ_v shows remarkable stability across the wide range of Ca/Si (1.0–2.0) [2]. Thus, suggesting that conventional stoichiometric modifications to C-S-H's molecular structure, such as altering its Ca/Si ratio, are not effective in modulating C-S-H's intrinsic thermal conductivity. It is because the heat transport in C-S-H is in the diffusive regime in which scattering dominates, i.e., the mean free path of phonons is in the order of a few Si—O bond lengths, which is significantly smaller than the C-S-H's nanoparticle size [2]. In this regime, the fractional contributions of propagating vibrational modes (propagons) and diffusive vibrational modes (diffusons) to the thermal conductivity of C-S-H are approximately 30 and 70 %, respectively [3]. Hence, it is worth asking if the thermal conductivity of C-S-H is already at its lowest achievable level, dubbed in the literature "glass limit" [5],

* Corresponding authors.
E-mail addresses: mjaq@uci.edu (M.J.A. Qomi), kjkrak@uh.edu (K.J. Krakowiak).

[1] These authors have contributed equally to this work.

[2] Currently at Wacker Chemical Corporation, NCA Innovation Ctr. & Regional Headquarters, 4950 S State Road, Ann Arbor, MI 48108, United States.

[3] Currently at Civil and Environmental Engineering Department, Massachusetts Institute of Technology, 77 Massachusetts Avenue, Cambridge, MA 02139, United States.

https://doi.org/10.1016/j.cemconres.2023.107324
Received 5 February 2023; Received in revised form 4 June 2023; Accepted 5 September 2023
Available online 9 September 2023

and if so, what new degrees of freedom are available to engineers to break this barrier while preserving strong, cohesive interactions at the nanoscale of cementitious materials [6,7].

The scattering of heat-carrying phonons impedes thermal transport in crystals and effectively reduces thermal conductivity [8,9]. Classically, the enhancement of phonon scattering is achieved by introducing a structural disorder to a crystal, e.g., the random atomic site substitutions in the lattice or the change of the conformational states to alter the vibrational motions of atoms [8]. However, new non-classical approaches, which couple organic and inorganic chemistry at the molecular scale, have emerged in recent years [10–12]. Indeed, Losego et al. [10] showed the thermal conductivity of organoclay nanolaminates, in which montmorillonite clay layers are intercalated with alkylammonium cations, displays cross-planar thermal conductivity that is 5-fold lower than that in unmodified clay composites, Fig. 1a. It was suggested that disparate acoustic properties of the organic phase and the montmorillonite phyllosilicate backbone, in conjunction with forming organic-inorganic interfaces, efficiently impede heat transfer in hybridized nanostructured layered materials. Inarguably, such examples demonstrate the potential mechanisms through which the organic-inorganic coupling produces ultralow-thermal conductivity materials. This technological path could potentially be adapted to cement science, Fig. 1b.

The examples of organic-inorganic coupling in C-S-H's molecular structure and texture have increasingly been reported in the cement chemistry literature [13–28]. However, most of these studies are concerned with the examination of polymer intercalation vs. adsorption of various organic molecules on its surface, as discussed in [29]. On the one hand, the primary motivation of these studies stems from the need to understand the mechanisms of interactions between superplasticizers, e.g., polycarboxylate ethers (PCEs) and cement hydration products [30]. On the other hand, their rationale is to explore the biomimetic control of C-S-H nucleation and growth to form organic-inorganic hybrids with enhanced toughness [31,32], akin to the nacre [33,34]. Regardless of the primary objective of these studies, they suggest that, in general, the hydrogen bonds or electrostatic forces govern the molecular-scale interactions in these organic-inorganic systems [35,36], which hinder direct chemical cross-linking between C-S-H layers [31,32]. Direct chemical cross-linking through Si—C covalent bond is only achieved using functionalized organometallics and sol-gel synthesis. This approach showed success in fabricating layered Al-, Mg-, and Ca-inorganic-organic nanocomposites [37], including C-S-H, in which continuous alkyl chains link opposite inorganic layers in nanoscale galleries [29,38–40]. Substantial data about the molecular structure of such novel composites exists. However, understanding the heat transport mechanism in organic-inorganic C-S-H hybrids is not yet adequate. Assumptions about the underlying molecular structure (prototypic models developed by Morshedifard et al. [4] assume the inorganic part of the molecular framework to follow 11 Å tobermorite while the experiments [29,37] point toward the brucite-like layered structure of portlandite to be more adequate) or, lack of experimental data on thermal properties at the relevant scale limit it.

In this work, building on the previously published results [4,29], we aim to address these severe experimental and modeling limitations and ultimately resolve the knowledge gap pertaining to the organic cross-linking effect on the intrinsic thermal conductivity of C-S-H nanolaminates. In particular, we seek to test the following hypothesis: "The cross-linking with functionalized organosilane molecules decreases conductive heat transport in C-S-H nanolaminates." A three-fold approach combining experiments, micromechanical modeling, and atomistic simulations is selected to test this hypothesis. On the experimental side, C-S-H nanocomposites of controlled stoichiometry and confirmed cross-linking are synthesized, fully dried, mechanically consolidated to various levels of packing density, and tested for effective thermal conductivity. However, the intrinsic thermal conductivity of C-S-H nanocomposites is estimated by solving the inverse problem using the self-consistent approximation of the effective medium theory [41]. We benchmark obtained estimates against the same Ca/Si ratio inorganic C-S-H reference solid. The atomistic simulations approach starts by constructing a realistic molecular-scale models of organic-inorganic C-S-H nanocomposites that are shown to be compatible with the molecular scale experimental data, including XRD, ^{29}Si NMR, ICP

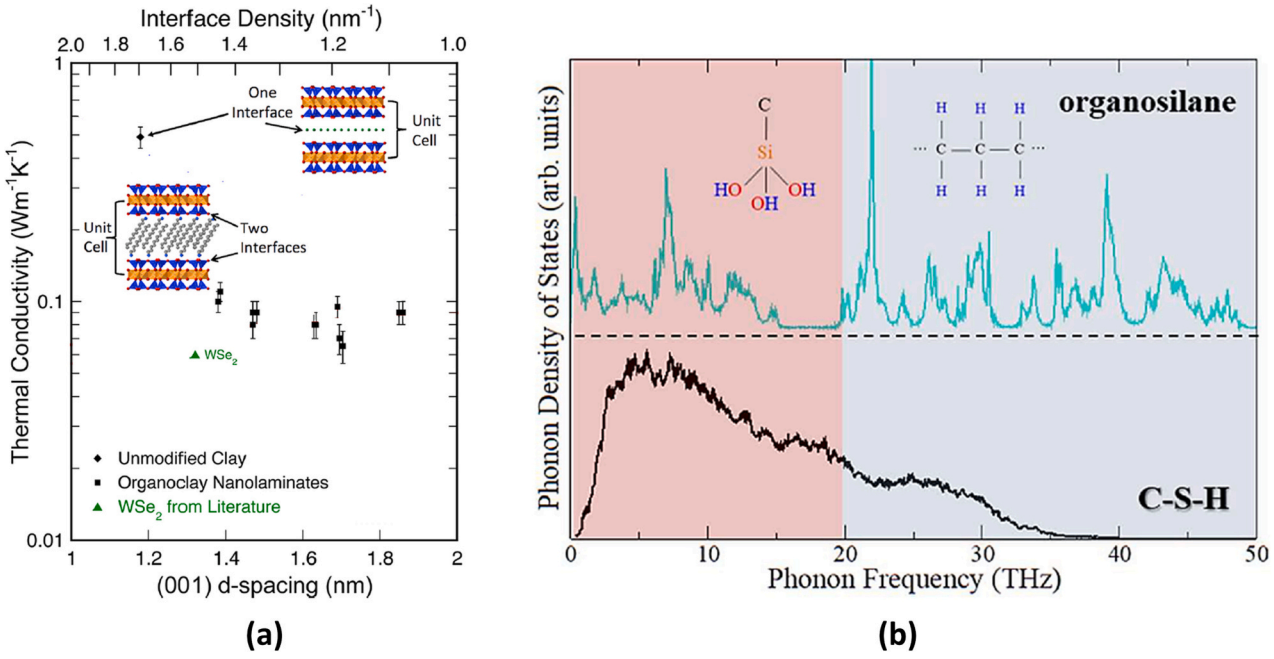

Fig. 1. Engineering of thermal conductivity via the organic-inorganic coupling. (a) The intercalation of inorganic sheets creates additional interfaces, which impede phonon transport and drastically reduce thermal conductivity in organoclay nanolaminates, modified after Losego et al. [10]. (b) Vibrational Density of States (VDOS) in C-S-H [3] and organosilane molecule; In C-S-H, the heat is carried by phonons with $\omega < 20$ THz, while in the organic counterpart, the heat is conducted through C—C bonds at phonon frequencies $\omega > 20$ THz. The VDOS mismatch between C-S-H and organic molecules is another mechanism that impedes the nanoscale heat transport in organic-inorganic nanolaminates.

spectrometry, and previously reported in Moshiri et al. [29]. Using the developed models, the thermal conductivity tensor is computed using the Green-Kubo formalism [2], followed by the scrutinized analysis of the phonon vibrational modes using the Allen-Feldman theory [42]. Finally, a section on the combined hypothesis testing and discussion of the heat transport mechanism in cross-linked organic-inorganic C-S-H nanocomposites and similar systems and a summary of main conclusions closes this work.

The novelty of this study is multi-fold:

a) It provides direct experimental and computational evidence of heat transfer impedance in organic-inorganic cross-linked C-S-H hybrids. If successfully realized technologically, e.g., hybrid nanoengineered admixture selectively interacting with cement native C-S-H, such organic-inorganic chemistry coupling could offer a new and alternative approach toward lowering the conductive heat transfer in cementitious composites beyond what classical approaches currently offer [43].
b) Guided by the experimental observations, this work proposes an original analytical and atomistic modeling strategy to decipher the effect of cross-linking on the thermal properties and structural organization of hybridized C-S-H at the molecular scale. Such models can aid in the molecular design of new admixtures for concrete.
c) Based on our knowledge, this work presents the first experimental study inferring the thermal conductivity of low-calcium C-S-H at the nanoscale, thus, providing critical input for multi-scale homogenization models of cement-based materials aiming at reliable prediction of thermal properties or, the mechanical performance of concrete structures subject to thermal loads.

2. Materials and methods

2.1. Combined experimental and analytical approach

2.1.1. C-S-H synthesis, conditioning, and molecular order

Inorganic and hybridized gels of controlled stoichiometry (target Ca/Si = 1) were prepared via the sol-gel route. The reference C-S-H was synthesized with tetraethoxysilane (TEOS, Sigma Aldrich), while the hybrid gels were functionalized with 1,6-BIS(Trimethoxysilyl)Hexane (Gelest Inc.), abbreviated here as HEX C-S-H, and 1,8-BIS(Triethoxysilyl)Octane (Gelest Inc.) abbreviated as OCT C-S-H. Before thermal conductivity investigation, solids were examined to confirm their molecular order. It included X-ray powder diffraction (Fig. 2a), thermogravimetry (Fig. 2b), chemical analysis through the inductively coupled plasma optical emission spectroscopy, as well as ^{29}Si and ^{13}C nuclear magnetic resonance and electron microscopy. A detailed discussion of the gel synthesis analytical protocols is included in the Supplementary information (SI), and experimental data on the molecular structure of cross-linked C-S-H is extensively presented in Moshiri et al. [29].

2.1.2. Density measurements via He-pycnometry

Density measurement of the inorganic and hybrid C-S-H solids was carried out in AccyPyc II Gas Displacement Pycnometer (Micromeritics, Norcross, USA). Before measurements, C-S-H gels were dried under vacuum at 50 °C for 24 h above the silica gel, followed by a standard convective oven drying at 105 °C to a constant weight. Prior to testing, the material was stored in vacuum-sealed tubes inside the desiccator. After a series of preliminary tests, the measurement parameters were optimized so that the helium expansion could reach equilibrium. For each sample, ten He-purges were performed, followed by five measurements of particle volume. The time for helium expansion was set to 500 s, and the purge and expansion pressure was 19.5 psig. The average sample weight for inorganic and hybrid C-S-H was 0.08 g and 0.04 g,

Basal spacing		
TEOS: C-S-H*	HEX: C-S-H	OCT: C-S-H
12.7 Å → 11 Å	14.1 Å	16.2 Å

Ca/Si molar ratio		
TEOS: C-S-H	HEX: C-S-H	OCT: C-S-H
1.02±0.03	0.93±0.07	1.02±0.03

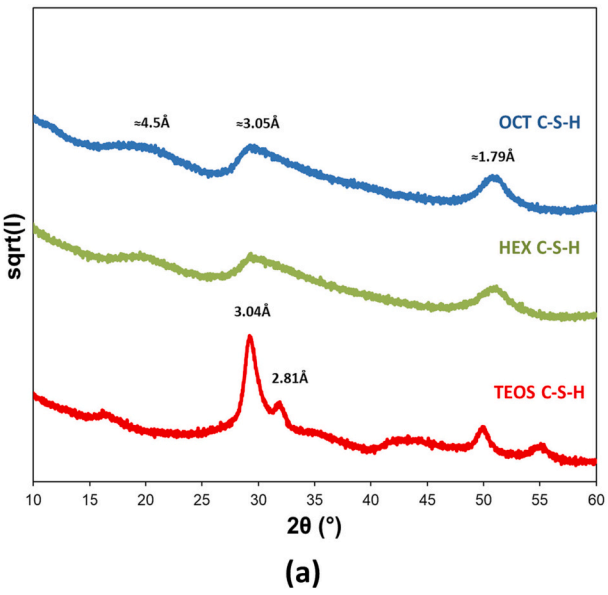

(a)

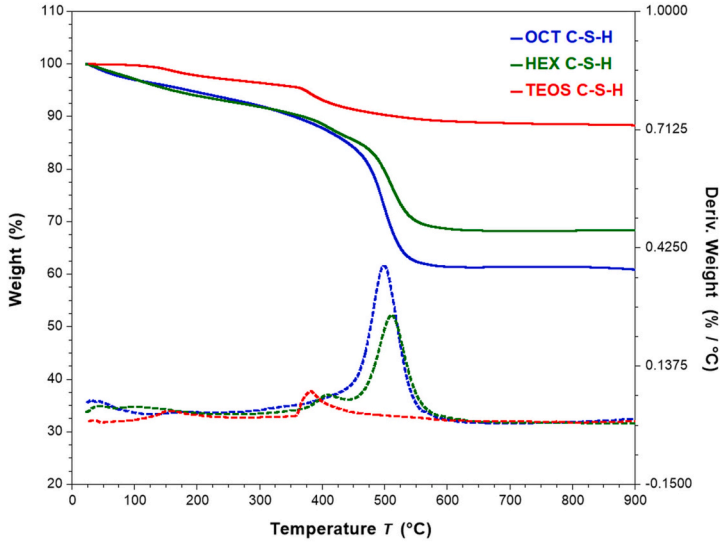

(b)

Fig. 2. Molecular scale characteristics of investigated cross-linked C-S-H nanolaminates and reference inorganic C-S-H gel. (a) XRD spectra of cross-linked C-S-H show attributes of the turbostratic structure established by randomly stacked layers of Ca-polyhedra. (b) Typical trends of weight loss in the TGA experiment under N_2 atmosphere on reference and hybrid gels dried at 105 °C and examined after thermal conductivity measurements. Diffraction and Ca/Si data after [29]. *- indicates the basal spacing shrinkage on drying from 50 to 105 °C in reference C-S-H sample. Dashed lines on panel (b) indicate weight derivative curves.

respectively. The expansion chamber volume was calibrated using AccuPyc™ NIST certified calibration standard, cross-checked with the borosilicate glass spheres and quartz sand, and the 0.1 cm^3 spacer was used in all measurements.

2.1.3. Powder consolidation and packing factor determination

Dry powders were ground using a high-speed ball mill (MTI Corporation, Richmond, USA). In each run, dry material was loaded into the 80 mL stainless steel jar with a set of steel spheres at the ball-to-solid weight ratio of 10:1. The grinding process took 1 h and ran in two segments (30 min each) with a 10 min stop between the segments. The pulverized material was sieved through a 75 μm mesh and later stored in the vacuum-sealed PVA containers inside the lab desiccator with dry silica gel.

All pellets were shaped in the 25 mm dry pressing die (Across International, Livingston, USA), Fig. 3. On average, around 4 g of material was loaded into the pressing die and compressed in the electromechanical universal testing machine (Instron, Norwood, USA) when the prescribed load was below 50 kN or servo-hydraulic system (MTS, Eden Prairie, USA) for higher loads up to 300 kN. The selection of the consolidation force required to achieve specific solid packing, η, spanning between 0.4 and 0.75, was based on the previously built master curves obtained in multiple preliminary trials run for each type of investigated solid.

2.1.4. Effective thermal conductivity measurements

The effective thermal conductivity of reference and cross-linked C-S-H pellets was measured with the heat flow meter FOX 50 (TA Instruments, 10 mm diameter transducer) following recommendations specified in ASTM standards C518 – 04 and E 1530 – 06 [44,45]. Across the entire testing campaign, the upper plate temperature was set to 25 °C, the lower plate to 15 °C, and the sample-transducer contact was realized via a pneumatic system operating at 35 psi (Fig. 4a). Transducers constants were calibrated on Pyrex reference material. A single-thickness measurement method was employed [46,47] supplemented with a variable thickness measurement for each C-S-H solid. Such an approach allows for a reliable estimate of the thermal contact resistance and delivers densely populated conductivity measurements in the packing density range from 0.4 to 0.75. Before measurements, each sample was re-dried at 105 °C in the light vacuum and placed inside the silica-filled desiccator at 1 % RH while in the queue for the thermal conductivity measurement.

The total contact resistance, 2Rc, was determined through the zero-intercept of the total thermal resistance vs. sample thickness method (Fig. 4b) [46,47]. For this purpose, three pellets of increasing thickness varying from around 3 mm to 6 mm, but with constant solid packing, were prepared and measured. The reproducibility of thermal measurements was checked by retesting the pellet in the "flipped" configuration (Fig. 4a).

2.1.5. Intrinsic thermal conductivity: analytical inference

The inference of the intrinsic thermal conductivity of reference and the hybrid C-S-H is carried out within the self-consistent (S—C) homogenization framework of the effective medium theory [41,48]. Accordingly, the pellets of synthetic C-S-H are treated as the composite material with polycrystalline-type morphology, see Fig. 5. A bi-phasic composite is defined by C-S-H solid particles, phase A, intermixed with air voids, phase B. Each phase is characterized by its intrinsic thermal conductivity, $\lambda^{(1)}$ and $\lambda^{(2)}$, and respective volume fractions $c^{(1)}$ and $c^{(2)}$, where $\sum c^{(i)} = 1$ [41]. Both phases are considered in perfect contact with zero particle-to-particle thermal resistance. The intrinsic thermal conductivity of C-S-H particles is treated as one of two unknowns and inferred in the inverse analysis. The thermal conductivity of air, phase B, is $\lambda^{(2)} = 0.026\ \mathrm{Wm^{-1}\,K^{-1}}$ [49]. The composite conductivity, λ^{eff}, is measured in the experiment at the pellet's bulk scale and at various C-S-H packing levels, η.

In the self-consistent approximation, in which spheroidal inclusions are isotropic and have uniform random orientations, the effective and phase conductivities relate through Eq. (1) [41]:

$$\sum_{i=1}^{N} c^{(i)} \left[\frac{2\left(\lambda^{(i)} - \lambda^{eff}\right)\lambda^{eff}}{\lambda^{eff}(1 - M_i) + \lambda^{(i)} M_i} + \frac{\left(\lambda^{(i)} - \lambda^{eff}\right)\lambda^{eff}}{2\lambda^{eff} M_i + \lambda^{(i)}(1 - 2M_i)} \right] = 0 \tag{1}$$

Here, M_i stands for components of the symmetric depolarization tensor expressed in the principal axes frame of the spheroidal inclusion [41]. For spheroidal inclusions with the semi-axes $a_1 = a_2 = a$ and a_3, depolarization tensor components are expressed through Eq. (2):

$$M_1 = M_2 = M = \frac{(1 - g)\gamma^2}{2(\gamma^2 - 1)} \tag{2}$$

where $= a_3/a$, and g for oblate shape $(\gamma < 1)$ is defined by Eq. (3) [41,50]:

$$g(\gamma) = \frac{1}{\gamma\sqrt{1 - \gamma^2}} arctan \frac{\sqrt{1 - \gamma^2}}{\gamma} \tag{3}$$

With λ^{eff} obtained in the direct experiment and the thermal conductivity of the gas phase known, the least square approach is adopted to

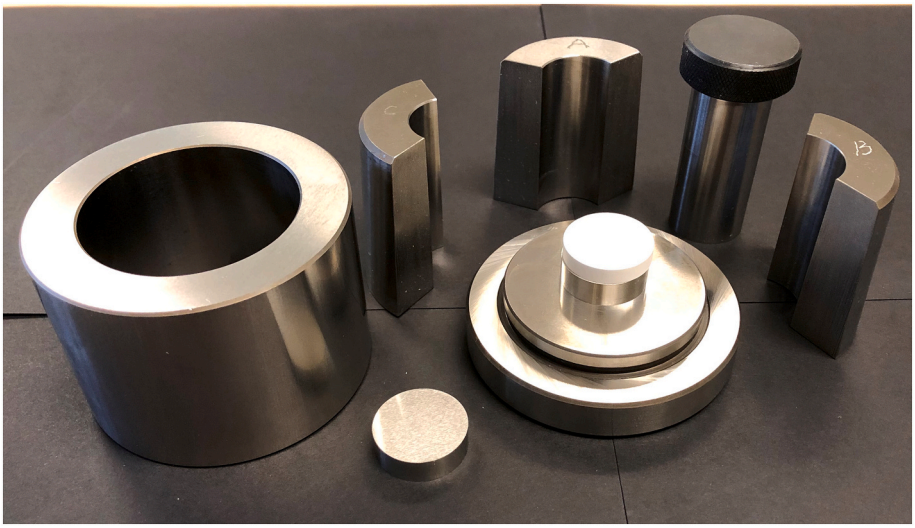

Fig. 3. Perspective view on the pressing die set for powder consolidation and pellet creation with TEOS: C-S-H reference pellet (white disk) after the consolidation.

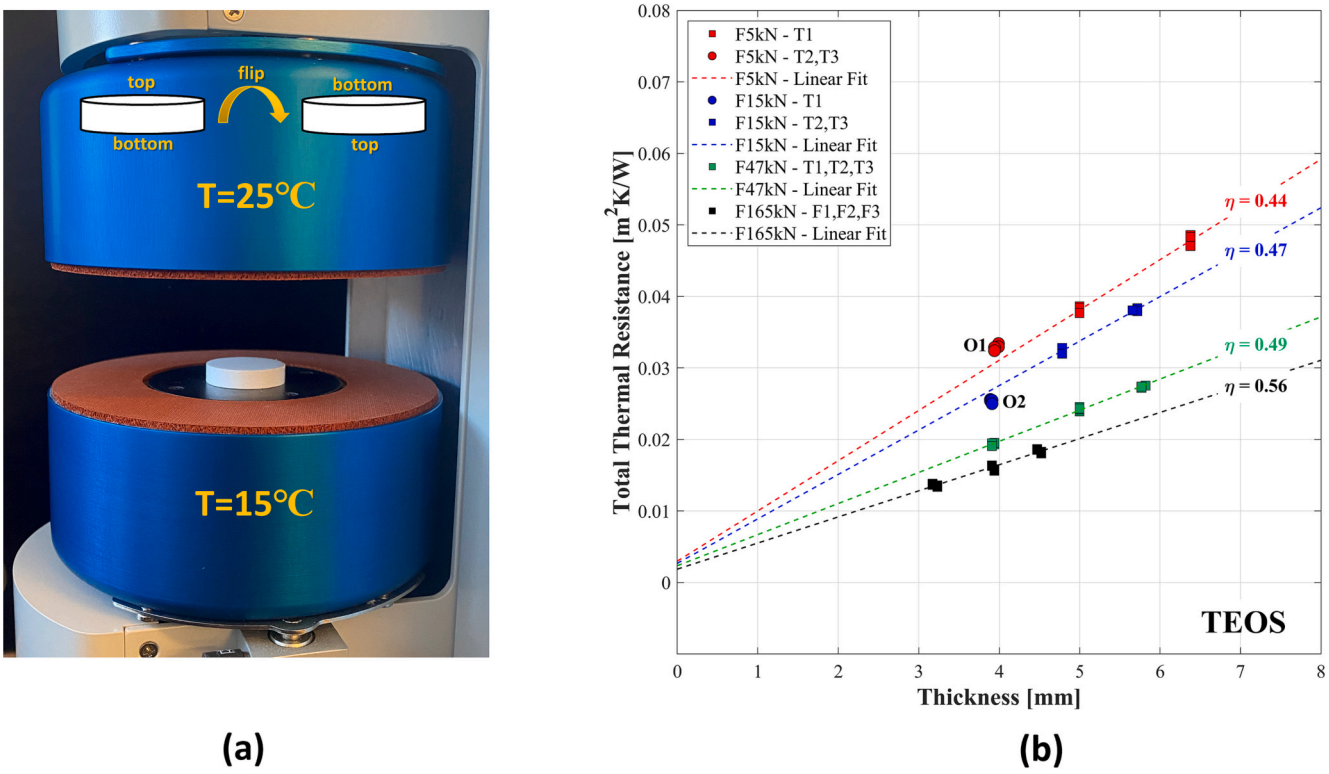

Fig. 4. Measurement of the effective thermal conductivity of consolidated C-S-H pellets: (a) perspective view on the pellet (φ = 25.4 mm) of consolidated C-S-H installed between the transducer plate of the heat flow meter before the testing, (b) construction of the total thermal resistance curves for the reference TEOS C-S-H used in the determination of the total contact resistance at zero-intercept. O1 and O2 experimental data points were excluded from the linear fit due to identified experimental error, which leads to grossly overestimated or unphysical negative contact resistance. Where η is packing density.

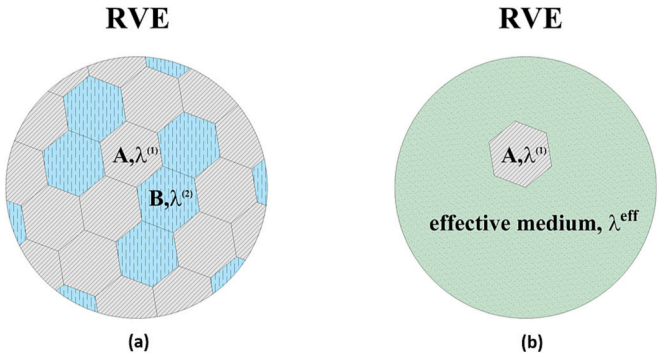

Fig. 5. The self-consistent approximation: (a) representative volume element (RVE) of the C-S-H pellet is modeled as a bi-phasic polycrystalline material with distinctive intrinsic thermal conductivities of phases, $\lambda^{(1)}$ and $\lambda^{(2)}$, (b) a single crystal of phase A immersed in an unbounded uniform medium with the effective thermal conductivity, λ^{eff}, measured in the heat flow meter experiment at various levels of solid packing.

solve the inverse problem and to infer two unknown parameters defined in S—C model through Eqs. (1)–(3) [51]. These are the intrinsic thermal conductivity of the solid phase, $\lambda^{(1)}$, and the void aspect ratio parameter, γ. Confidence intervals on estimated parameters were generated using the Monte-Carlo approach [52] programmed in Wolfram Mathematica.

2.2. Atomistic modeling approach

2.2.1. Structural models

To test our hypothesis using molecular simulations, we constructed realistic molecular structures of cross-linked C-S-Hs on the structural framework of portlandite. This choice of the molecular archetype is guided by the totality of experimental data reported by the authors in [29] e.g., powder X-ray diffraction, ^{29}Si NMR, ICP spectrometry. Moreover, the available literature on the sol-gel derived (Al, Mg, Ca)-alkyl silicates [37–40], which can serve as possible analogs to our systems, suggest the formation of brucite-like layers similar to the one found in portlandite.

First, we constructed an orthogonal supercell of portlandite by transforming the cell vectors of its primitive cell as follows, Eq. (4):

$$\begin{bmatrix} \mathbf{a} \\ \mathbf{b} \\ \mathbf{c} \end{bmatrix} = \begin{bmatrix} 3 & 0 & 0 \\ 1 & 2 & 0 \\ 0 & 0 & 1 \end{bmatrix} \begin{bmatrix} \mathbf{a}_{prim} \\ \mathbf{b}_{prim} \\ \mathbf{c}_{prim} \end{bmatrix} \tag{4}$$

where for portlandite, the primitive cell vectors are $\mathbf{a}_{prim} = (3.59,\ 0.00,\ 0.00)$, $\mathbf{b}_{prim} = (-1.80, 3.11, 0.00)$ and $\mathbf{c}_{prim} = (0.00,\ 0.00,\ 4.91)$ [53], which after the above transformation gives an orthogonal unit cell with parameters $a = 10.78$ Å, $b = 6.22$ Å, $c = 4.91$ Å and $\alpha = \beta = \gamma = 90°$. Next, three dipodal organosilanes are joined through their tetrahedral silicates to form an organosilane trimer, as shown in Fig. 6a. These trimers are grafted to portlandite layers, which form a cross-linked organic-inorganic structure. The interlayer space required for the process is estimated based on the expected polymer length. The cell height is increased to 14 Å in the case of hexane and to 16 Å in the case of octane, Fig. 6a. This arrangement resulted in a structure that is close to an energy minimum and can be optimized with the density functional theory (DFT) technique (Fig. 6b) [54]. The hybrid structures constructed achieve Ca/Si = 1 and $T^1/(T^1 + T^2) = 0.67$, which is satisfactory when compared to experimentally measured $T^1/(T^1 + T^2)$ of 0.57 and 0.71 for hexane and octane C-S-H, respectively, and as reported by Moshiri et al. [29].

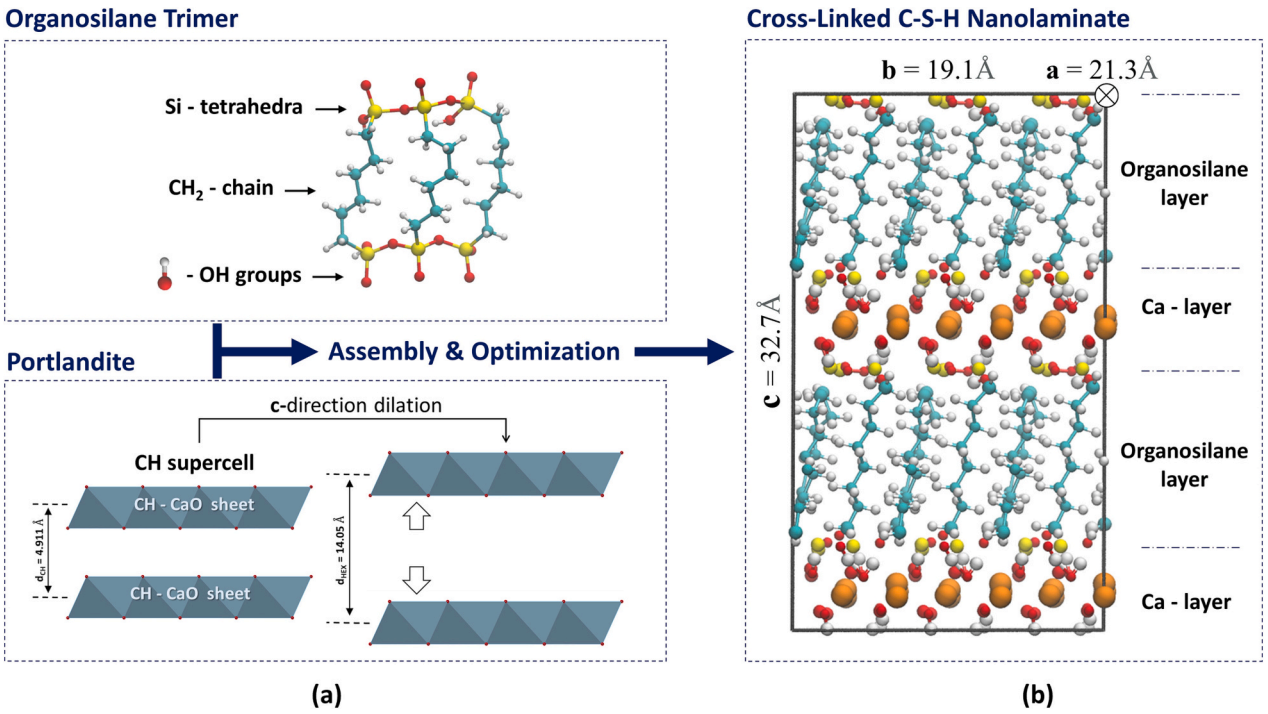

Fig. 6. The construction of representative cross-linked C-S-H models: (a) portlandite supercell and organosilane trimer, (b) The hybrid structure after energy optimization using periodic DFT calculations. Cell dimensions are a = 21.3 Å, b = 19.1 Å, and c = 32.7 Å.

2.2.2. Dispersion-corrected DFT optimization

Periodic density functional theory (DFT) [54] calculations were carried out using the VASP simulation package [55]. The energy cutoff was set to 600 eV for the plane wave basis set. The projector wave method [56] is used in our calculations. Moreover, Grimme's D2 method [57] accounted for dispersive interactions between atomic species in the system. Based on the system size, a 2 × 2 × 1 grid of kpoints was adopted to sample the Brillouin zone. When the system setup is complete, the ionic positions are relaxed using the conjugate gradient optimizer. The convergence criterion was set on forces where |F max | = 0.001 eV/Å.

After initial setup, the system was energetically minimized for both atomic and cell degrees of freedom (DoF) using the conjugate gradient optimizer as implemented in VASP. Although the initial atomic configuration created based on experimental data should be close to an energy minimum, we found that the optimization needed to be carried out in stages for the system to settle into a high-quality minimum. After several iterations, the following scheme was adopted for structural optimization. First, the atoms in the layer (calcium, silicon and oxygen) are frozen during the initial minimization. This is to avoid spurious distortion of the layers and allow the polymers to relax. Moreover, cell shape and volume are fixed. Second, oxygen and silicon atoms are allowed to move while calcium atoms are still frozen. In this step, cell volume and shape are also allowed to vary. Finally, full optimization is performed during which all atoms and cell shape/volume are allowed to vary.

2.2.3. MD-based thermal conductivity inference

Although DFT simulations provide accurate athermal structures for the material, they put severe spatial and temporal limitations on finite temperature simulations, which makes them unsuitable for thermal conductivity calculations. ReaxFF [58] or classical force fields are viable routes for simulating our system. However, ReaxFF is mainly geared toward modeling reactive systems, while our study focuses on heat transfer, which does not involve bond breaking/forming. A non-reactive forcefield would suffice because the structure is already derived using experiments and DFT calculations. Moreover, Green-Kubo simulations for thermal conductivity calculations are computationally expensive. Since ReaxFF is about an order of magnitude slower than classical forcefields, carrying out the simulations with moderate available resources would be challenging. Finally, it's not clear how accurate ReaxFF would be with regard to phonon calculations since they require fitting to second-order data, such as elastic and/or vibrational data for the particular system under study. To the best of our knowledge, such data are not available yet. Considering these facts, ReaxFF can be ruled out for the system in this study.

Furthermore, experiments have demonstrated that the molecular framework of inorganic component in our system is portlandite-like rather than C-S-H [29]. The ClayFF potential was developed with portlandite as part of its fitting dataset [59]. Moreover, it has been shown that ClayFF gives accurate second order properties for portlandite [60]. Regarding the addition of the organic part, ClayFF was originally developed for compatibility with the Consistent Valence force field (CVFF, [61]) and also uses the flexible SPC water model. (see [62] for further discussion by the developers of the force field). Hence, a number of publications ([63–65] among others) have successfully verified/utilized ClayFF+CVFF for hybrid organic/inorganic structures.

Based on the above discussion, in this study, we use a combination of ClayFF [58,59] and CVFF [61,66,67] for the inorganic and organic parts of the system, respectively. The charge of the silicon connected to the polymer was derived using a charge neutrality constraint.

A supercell is constructed from the relaxed unit cells obtained from DFT. The systems have 1152 and 1368 atoms for C-S-H HEX and C-S-H OCT, respectively. We use LAMMPS simulation package for all computations [68]. All models in our numerical experiments are initially relaxed in the NPT ensemble using Nose-Hoover thermostat [69] at 300 K and Parinello-Rahman barostat [70] at 1 atm for 1 ns and time steps of 1 fs.

The thermal conductivity tensor ($\boldsymbol{\lambda}$) is subsequently computed using the so-called Green-Kubo formalism [2]:

$$\boldsymbol{\lambda} = \frac{V}{k_B T^2} \int_0^\infty \langle \mathbf{J}(0) \otimes \mathbf{J}(t) \rangle \, \mathrm{d}t \tag{5}$$

where $\mathbf{J}$ is the heat flux vector, k_B is the Boltzmann factor, T is

temperature and V is the simulation cell volume; see Qomi et al. [2] for more detail. Heat flux is collected every femtosecond in an NVT run of 10 ns.

Based on their spatial characteristics, we classify vibrational modes as localized (locons), wave-like (propagons), and those with random spatial spread (diffusons). The total thermal conductivity can be decomposed as $\lambda = \lambda_{\text{prop}} + \lambda_{\text{diff}} + \lambda_{\text{loc}}$, where the terms on the right-hand side are propagon, diffuson and locon contribution to conductivity. We compute the contribution of diffusons using the Allen-Feldman theory [42] as follows:

$$\lambda_{\text{diff}} = \frac{1}{V}\sum_i C_i(T) D_i \tag{6}$$

where the summation is over each vibrational mode and the mode diffusivity is:

$$D_i = \frac{\pi V^2}{3\hbar^2 \omega_i^2} \sum_j^{\neq i} |S_{ij}|^2 \delta(\omega_i - \omega_j) \tag{7}$$

Here, C_i is the heat capacity of mode i, S is the heat current operator, V is the cell volume and ω_i is the frequency of mode i. We use GULP software [71] for calculating vibrational modes and their diffusivities in inorganic and cross-linked C-S-H systems.

2.2.4. Modal analysis

This work calculates the vibrational density of states (VDOS) using the Fourier transform of velocity autocorrelation obtained from an MD run in the microcanonical (NVE) ensemble [2]:

$$g(\omega) = \frac{1}{Nk_B T} \sum_{j=1}^{N} m_j \int_{-\infty}^{\infty} \langle \mathbf{v}_j(t) \cdot \mathbf{v}_j(0) \rangle e^{i\omega t} \mathrm{d}t \tag{8}$$

where N is the number of atoms, m_j and $\mathbf{v}_j$ are mass and velocity vector of atom j.

To further understand the mechanisms underlying heat transport in the cross-linked C-S-H, vibrational modes and frequencies are obtained from eigenvalues and eigenvectors of the dynamical matrix as implemented in GULP package [71]:

$$D_{pq,\alpha\beta}(k) = \frac{1}{\sqrt{m_p m_q}} \left(\frac{\partial^2 U_{\text{lat}}}{\partial \alpha \partial \beta} \right) e^{ikr} \tag{9}$$

p and q denote the atoms, α and β are the Cartesian coordinate indices, $\mathbf{D}$ is the dynamical matrix, m_p is the mass of the p^{th} atom, U_{lat} is the lattice internal energy, and e^{ikr} is the phase factor. The eigenvalue problem $(\mathbf{D} - \omega^2 \mathbf{I})\boldsymbol{\varepsilon} = 0$ can be solved to find the vibrational frequencies ω_i and vibrational modes $\boldsymbol{\varepsilon}$.

To distinguish localized modes (locons), we compute participation ratio for each mode [72]:

$$P^j = \frac{1}{N \sum_{i=1}^{N} |\boldsymbol{\varepsilon}_i^j|^4} \tag{10}$$

where $\boldsymbol{\varepsilon}_i^j$ is the polarization vector of atom i in mode j, noting that $\sum_{i=1}^{N} |\boldsymbol{\varepsilon}_i^j|^2 = 1$. We assign modes with $P^j < 0.05$ as locons.

To distinguish propagons, we use the method proposed by Morshedifard et al. [4]. For each non-localized mode, we compute the spatial Fourier transform as:

$$\gamma^k(\mathbf{k}_r) = |\sum_{j=1}^{N} \sum_{\alpha=1}^{3} \varepsilon_{j\alpha}^k(\mathbf{r}_j) e^{-i\mathbf{k}_r \cdot \mathbf{r}_j}| \tag{11}$$

where $\varepsilon_{j\alpha}^k$ is the α component of polarization vector of atom j and $\mathbf{k}_r$ is r^{th} wavevector in k-space and $\gamma^k(\mathbf{k}_r)$ is the amplitude of the sum of Fourier transforms of each component of eigenvector k for wavevector $\mathbf{k}_r$. To capture modes that are "wave-like" and hence propagating, we compute the absolute value of the standard score, also known as the z-score [73]:

$$z_r^k = \left| \frac{\gamma^k(\mathbf{k}_r) - \mu^k}{\sigma^k} \right| \tag{12}$$

where μ^k and σ^k are the mean and standard deviation of the dataset for mode k. In this study, modes with a z-score >6 are considered propagating.

3. Results

3.1. Solid particle density

3.1.1. Experimental density of reference and cross-linked C-S-H

The experimental estimates of the solid density based on the He-pycnometry are presented in Table 1. With regard to the reference C-S-H solid, the measured density increases with the increase in solid dehydration caused by increasingly more severe drying from 50 °C to 105 °C. A similar trend is observed for the cross-linked C-S-H regardless of the length of the organic alkyl chain. The measured density of reference C-S-H, ≈1.9 g/cm^3, is significantly below the theoretical densities expected for closely related mineral systems such as tobermorite and jennite groups [74]. For example, in the tobermorite group, the 14 Å tobermorite (plombierite, Ca/Si = 0.83) displays the lowest theoretical density between 2.23 (monoclinic) to 2.28 g/cm^3 (orthorhombic), while jennite's (Ca/Si = 1.5) density is 2.33 g/cm^3, respectively. Both minerals have been considered structural end-type archetypes of the calcium-silicate-hydrate gel [74–77]. This indicates that in the current experiment, the He is overestimating the C-S-H solid volume. This effect may be the result of the presence of residual water molecules in gel dried at 50 °C, or occluded nano-porosity caused by the C-S-H agglomeration and collapse, Fig. 7. Both phenomena restrict the transport of gas molecules. The first mechanism is corroborated by the interlayer distance of ≈12.6 Å [29] as measured in the powder XRD experiment and an additional weight loss on drying from 50 °C to 105 °C to a constant weight. This interlayer spacing indicates a C-S-H between lightly and severely dried states as noted by Richardson [75]. Upon more severe drying, the C-S-H interlayer space collapses to ≈11 Å [29], which indicates more pronounced dehydration. However, only a minor increase in the measured density is observed, suggesting a severe underestimation of the true particle density in the complete dried state, Table 1. In consequence, such systematic error would lead to grossly overestimated packing of C-S-H in prepared pellets for the solid thermal conductivity measurements.

3.1.2. True solid density of C-S-H in 105 °C dry state

As an alternative to He-based measurements in Table 1, the solid particle density of reference C-S-H gel (Ca/Si = 1), in the complete dry state, is estimated through a combination of the approach outlined by

Table 1
Density of the reference and cross-linked C-S-H solids measured in He-pycnometry.

	Solid type					
	TEOS: C-S-H		HEX: C-S-H		OCT: C-S-H	
Drying T[a]	50 °C	105 °C	50 °C	105 °C	50 °C	105 °C
ρ (g/cm^3)	1.90 ± 0.01	1.96 ± 0.02	1.58 ± 0.02	1.71 ± 0.02	1.52 ± 0.01	1.58 ± 0.02
d_{002} [Å]	12.69	10.84	14.05		16.20	
$[CH_2]_n$ size	NA		6		8	

[a] 50 °C drying under light vacuum above silica gel for 24 h, additional drying at 105 °C in conventional oven.

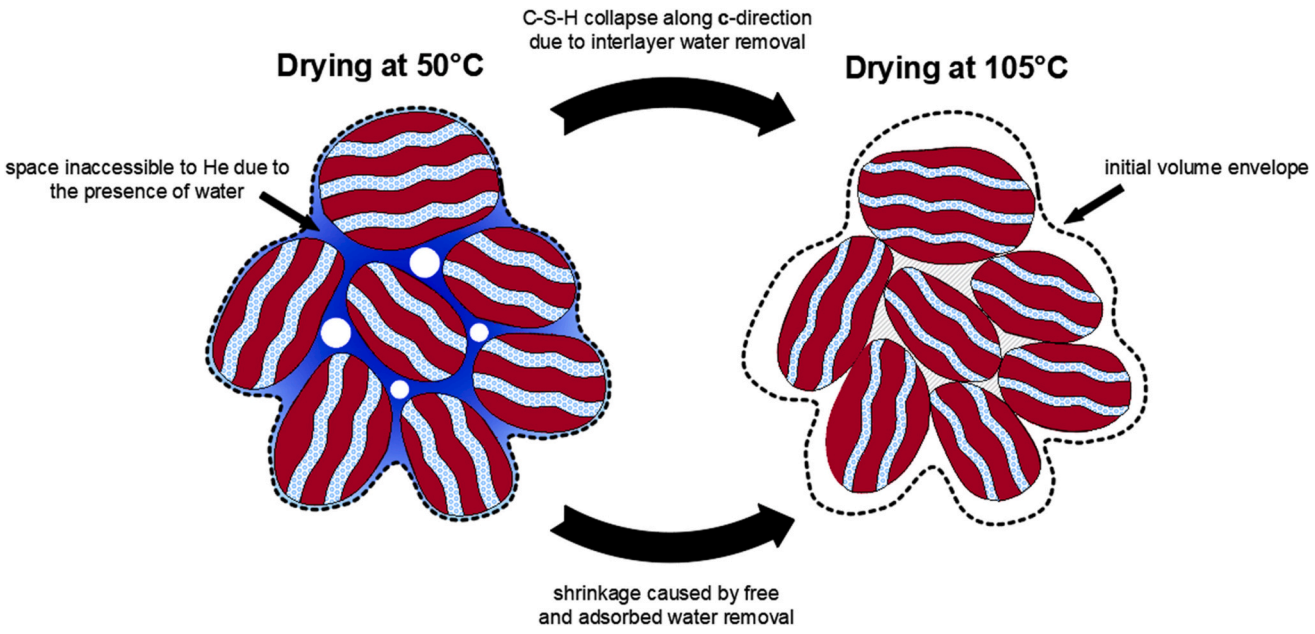

Fig. 7. Conceptual schematic of the particle rearrangement in C-S-H gel upon drying and its effect on the gel's volume measurement. The presence of residual free and adsorbed water on the particles surface effectively increases measured volume by reducing free volume for gas permeation. Harsh drying leads to C-S-H rearrangements and particle agglomeration, resulting in shrinkage and occluded nanoporosity (hatched gray) that is inaccessible to He.

Thomas et al. 2010 [77] and X-ray diffraction measurements [29]. Accordingly, starting from the structure of 14 Å tobermorite ($C_{0.83}SH_{1.33}$, $\rho = 2.23$ g/cm^3), which is considered the mineral analog to low calcium C-S-H [75,77], the molar volumes of CaO and H_2O necessary to convert 1 mol of tobermorite to reference C-S-H is calculated. Thus, 0.17 mol of CaO must be added to the tobermorite molecular formula to increase the Ca/Si ratio from 0.83 to 1 (measured in ICP-OS, Fig. 2, [29]). Given its molar volume (MV) of 16.79 cm^3, the volume occupied by added CaO is 2.854 cm^3. On the other hand, the necessary volume change due to H_2O equals −13.243 cm^3. The negative volume reflects the tobermorite unit cell contraction along **c**-direction from the initial 14 Å to 10.84 Å. The latter value corresponds to the d_{002} basal spacing measured in XRD experiment on 105 °C dried TEOS: C-S-H samples, Table 1. This volume estimate assumes water MV = 18.05 cm^3, which implies H_2O density of 0.9982 g/cm^3, a value representing the density of bulk water at 20 °C.

According to recent MD studies investigating C-S-H's composition-dependent dynamics of nanoconfined water in the interlayer space [78], the bulk water type behavior may be assumed for low lime C-S-H. This is in contrast to the high Ca/Si = 1.75 ratio typical of C-S-H developed during cement hydration [1], in which the interlayer water is considered as "compressed" with $\rho = 1.1$ g/cm^3 [77,78]. Therefore, the conversion of 1 mol of 14 Å tobermorite with MV = 58.67 cm^3 to 1 mol of TEOS: C-S-$H_{0.6}$, requires net volume reduction of $\Delta V = -10.39$ cm^3 (17.71 %). Consequently, the calculated solid particle density of reference C-S-H gel is between 2.60 and 2.63 g/cm^3 depending on the crystal system of starting 14 Å tobermorite, and/or interlayer water density, respectively. Interestingly, this estimate is very close to the density of clinotobermorite (Ca/Si = 0.83, H/S = 1, $d_{002} = 11.3$ Å), which is 2.611 g/cm^3. This estimate is also below the limiting density of 9 Å tobermorite, 2.864 g/cm^3 [74], and the density of a single C-S-H sheet with all evaporable water removed, 2.85 g/cm^3 [79].

3.1.3. Cross-validation of particle density of hybrid C-S-H gels

Given that the He-pycnometry systematically underestimated the reference C-S-H density, we cross-validate the measured values (Table 1) for the hybrid gels. Such twofold cross-validation includes (a) the analytical estimation of theoretical solid density considering quantitative metrics obtained from other independent experiments assessing molecular order of cross-linked gels, e.g., NMR and (b) the density estimate from our independently developed atomistic models.

The theoretical estimation of the particle density of cross-linked C-S-H is based on the modified molecular structure derived from the portlandite (CH) mineral.

The construction of simplified analytical first-order model starts from the dilation of the original unit cell of CH along **c**-crystal direction to account for increased basal spacing measured via XRD in organic-inorganic C-S-H gels (Fig. 6a, lower panel). Naturally, this operation increases the volume occupied by hybrid solid, V_{HYB} (Eq. (13)), where λ is the ratio of interlayer distance in hybrid C-S-H to interlayer spacing in CH, and V_{CH} is the original volume occupied by CH solid.

$$V_{HYB} = \lambda \times V_{CH} \tag{13}$$

Next, the -Si-$[CH_2]_n$-Si- organometallic chains are condensed within the interlayer space to form a cross-linking monolayer. After condensation, each molecule has 4^+ charge surplus that is associated with the missing hydroxyl groups in terminal Si tetrahedra, e.g., $(Si_2[CH_2]_6)^{4+}$ for HEX: C-S-H. The stoichiometric amount of organosilane molecules must match the Ca/Si molar ratio determined in the OS-ICP experiment [29], (Fig. 2). As a result, the combined mass of inorganic CH backbone and organometallic molecules occupying V_{HYB} is, Eq. (14):

$$m_1 = \rho_{CH} V_{CH} \left(1 + \frac{1}{2\beta} \frac{M_{ORG}}{M_{CH}}\right) \tag{14}$$

where ρ_{CH} is the density of portlandite 2.21 g/cm^3, β is the Ca/Si ratio of hybrid C-S-H, Fig. 2, M_{CH} is the molar mass of portlandite, M_{ORG} is the molar mass of the organometallic insert, which is 140.33 and 168.38 g/mol for $(Si_2[CH_2]_6)^{4+}$ and $(Si_2[CH_2]_8)^{4+}$, respectively.

The number of OH^- groups and O^{2-} ions required to balance the charge is added in the amount compatible with the measured abundance of T^1 and T^2 species. To elaborate more, each T^1 type unit present at terminal sites of silica chain, or in simple dimer structures, must be connected to one hydroxyl group. However, this group is absent in T^2 species (Fig. 8). Additionally, the condensation reaction involves the creation of siloxane links between adjacent organosilane molecules, therefore, the fractional contribution of O atom is ½ for T^1 (single -Si-O-

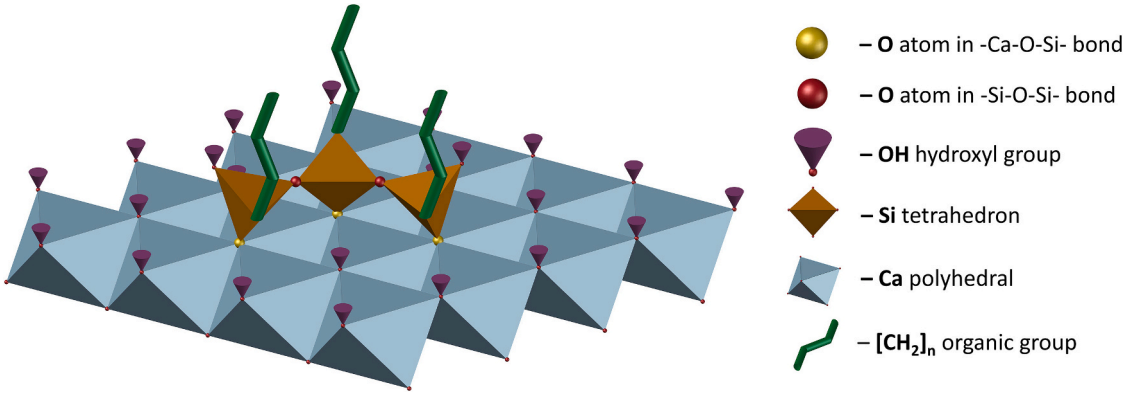

Fig. 8. Schematic of Si-trimer type structure condensing on the single CH sheet. All structural dimensions are in scale. For the sake of clarity, the organic chain is limited to a small portion of its total length.

Si- link) and 2 × ½ for T^2 (two -Si-O-Si- links), respectively (Fig. 8). Given this, the required amount of hydroxyl groups, m_{OH}, and oxygen participating in siloxane groups, m_O, is determined according to Eqs. (15a) and (15b).

$$m_{OH} = Q_{T^1}\rho_{CH}V_{CH}\frac{1}{\beta}\frac{M_{OH}}{M_{CH}} \tag{15a}$$

$$m_O = (0.5Q_{T^1} + Q_{T^2})\rho_{CH}V_{CH}\frac{1}{\beta}\frac{M_O}{M_{CH}} \tag{15b}$$

To ensure this hybrid system is charge neutral, we adjust for the number of H atoms (m_H) that are part of OH groups of the original CH sheet, Eq. (16), and must be removed to allow for the condensation of Si-tetrahedron onto the CaO polyhedral layer, Fig. 8.

$$m_H = \rho_{CH}V_{CH}\frac{1}{\beta}\frac{M_H}{M_{CH}} \tag{16}$$

Finally, we calculate the density of the cross-linked C-S-H gel accounting for the aforementioned mass sources:

$$\rho_{HYB} = \frac{m_1 + m_{OH} + m_O - m_H}{V_{HYB}} \tag{17}$$

We follow the outlined procedure to estimate the theoretical density of cross-linked C-S-H hybrids investigated in this work, Table 2. Despite simplifications of the presented analytical model quite remarkable agreement is observed (relative error < 5 %) between the analytical estimates and experimental measurements obtained on HEX: C-S-H and OCT: C-S-H gels with He-pycnometry.

Finally, the confidence in the experimentally determined solid densities of cross-linked C-S-H is further strengthened by DFT-based estimates, and is reflected by the small relative error of <5 %, Table 2. Such an agreement additionally supports the adequacy of the atomistic model, which is used in the inference of the heat conductivity and the associated molecular mechanism. MD-based inference of thermal properties was carried out in synergy with the experimental campaign to test the postulated hypothesis. We note that to enhance the treatability of the atomistic approach and to streamline the MD simulations process, the proposed molecular structures of cross-linked C-S-Hs (Fig. 6) are constructed to achieve Ca/Si = 1 and T^1 / (T^1 + T^2) = 0.67, regardless the size of organosilane molecule. These parameters are in close agreement with our earlier characterization experiment performed by Moshiri et al. [29]. A certain level of discrepancy between simulations and experiments is inevitable that is slightly more pronounced in HEX: C-S-H type solid.

3.2. Experimental inference of thermal conductivity

3.2.1. Reference C-S-H

We present the results of the heat flow experiments on the consolidated reference C-S-H pellets in Fig. 9. As expected, we recover the classical trend [8,80]; i.e., the effective thermal conductivity increases with increasing C-S-H's packing density or, otherwise said, with decreasing its porosity.

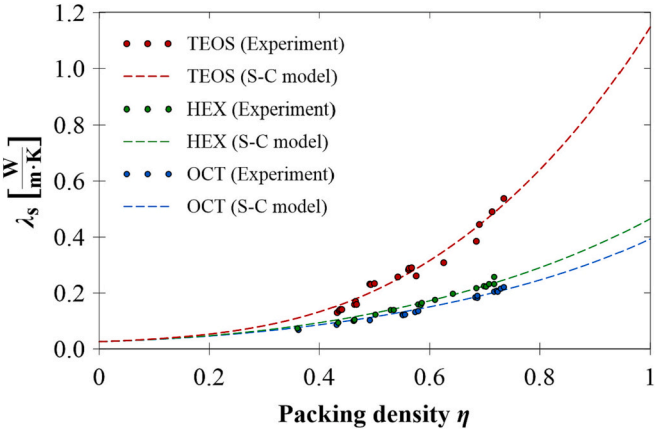

Fig. 9. Experimentally measured effective thermal conductivity of consolidated reference (TEOS) and cross-linked (HEX and OCT) C-S-H pellets vs. the solid packing density. Data is accompanied by the respective optimum fits of the S—C model obtained by solving the inverse problem. The extrapolation to $\eta = 1$ gives the intrinsic thermal conductivity of C-S-H.

Table 2
Theoretical and DFT-based estimates of the particle density of hybrid C-S-H gels.

Gel type	Parameter/metric							Model ρ (g/cm^3)	DFT ρ (g/cm^3)	ε (%)[b]
	n	λ	T^1:T^2	m_1	m_{OH}	m_O	m_H			
HEX: C-S-H[a]	6	2.87	60:40	4.460	0.327	0.359	0.032	1.78	1.71	<5 (1)
OCT: C-S-H[a]	8	3.30	70:30	4.672	0.348	0.304	0.029	1.60	1.62	<2 (3)

[a] T^1:T^2 ratio after ref. [29].
[b] Relative error w.r.t experimental values determined in He-pycnometry, Table 1, values in parenthesis represent the relative error between DFT and experiment.

The optimum fit of the S—C model, Fig. 9, predicts the intrinsic thermal conductivity of the reference C-S-H solid to be equal to 1.15 ± 0.1 Wm^{-1} K^{-1} and the 95 % confidence interval 0.95–1.35 Wm^{-1} K^{-1}, see Fig. 10a. Furthermore, λ_s has asymmetric distribution as indicated by the slight divergence from the linear trend in the Q-Q plot, Fig. 10b. To the author's knowledge, this is the first direct experimental inference of the semi-crystalline C-S-H's (Ca/Si = 1) intrinsic thermal conductivity at the nanoscale. The available literature data have only been restricted to those estimated via atomistic simulations [2–4,81,82]. Accordingly, the reported MD estimate of volumetric thermal conductivity of semi-amorphous C-S-H at Ca/Si = 1.75 ranges from 0.94 [3] to 0.98 Wm^{-1} K^{-1} [2], with differences resulting from variations in the technical aspects of the MD approach. The thermal conductivity of 11 Å tobermorite is also reported to be 1.29 ± 0.08 Wm^{-1} K^{-1} [4]. Additionally, based on the inverse analysis of the experimental data obtained on the hydrated cement paste by Bentz [83], Zhou et al. [3] estimated the thermal conductivity of C-S-H at Ca/Si = 1.7 to be 0.95 ± 0.25 Wm^{-1} K^{-1}. Our S—C estimate and MD-based predictions for semi-amorphous C-S-H are quite closely aligned, which further supports the overall validity of molecular structures developed in prior works by the authors [2–4,76].

3.2.2. Cross-linked C-S-H hybrids

Our experimental results on the correlation of the effective thermal conductivity of cross-linked C-S-H hybrids (HEX and OCT) pellets and the solid packing are benchmarked against the reference C-S-H (TEOS) in Fig. 9. In both cases, the modification of C-S-H's molecular framework with the bis-organosilanes significantly reduces the effective thermal conductivity across the entire domain of packing density. Furthermore, the observed decrease correlates with the molecular weight of the cross-linking agent, which is the function of the CH_2 linear chain length in this case. Thus, the trend in the effective thermal conductivity of the OCT: C-S-H (n = 8) is systematically below the one recorded for HEX: C-S-H (n = 6). The extrapolation of the S—C model to $\eta = 1$ (see Fig. 9) gives solid thermal conductivity 0.47 ± 0.02 Wm^{-1} K^{-1} and 0.39 ± 0.01 Wm^{-1} K^{-1} for HEX and OCT: C-S-H, respectively. In both cases, distributions are asymmetric. However, their divergence from the normal distribution tends to be reduced (see Fig. 10a and b) compared to the reference C-S-H (TEOS).

3.3. MD-based inference of thermal conductivity and the heat transport mechanism

We utilize the Green-Kubo formalism, as described in the Materials and methods section (Eq. (5)), to compute the volumetric thermal conductivity of HEX: C-S-H and OCT: C-S-H that are respectively $\lambda_v = 0.83$ ± 0.05 Wm^{-1} K^{-1} and λ_v = 0.69 ± 0.05 Wm^{-1} K^{-1}. Similar to the experiment, we see a meaningful reduction in thermal conductivity as the polymer chain length increases. We aim to investigate the origins of the decrease in thermal conductivity. Based on previous studies, we can conclude that the main factor is the scattering of heat carriers at the interface between the organic/inorganic constituents [12,84–86]. Such interface effects can be best studied in simple models such as superlattices [87]. For example, in the case of Si/Ge superlattices, it can be shown that a mismatch in VDOS between Si and Ge results in the observed Kapitza resistance at the interface, which in turn results in reduced thermal conductivity [88]. Moreover, it was shown that the Kapitza effect is more pronounced in the amorphous case, which is similar to the condition at the organic/inorganic interface in this study.

We can compute vibrational density of states (VDOS) using the Fourier transform of velocity autocorrelation as described in Eq. (8). Moreover, the partial contributions from atomic species can also be computed to better understand the VDOS curve. As seen in Fig. 11, we observe a mismatch between contributions from the polymer and the inorganic portlandite in the frequency range 35 THz ~ 50 THz. Previous research on solid-solid interfaces has shown that such vibrational mismatch results in a reduced thermal conductivity [89]. There exist theoretical models such as the acoustic mismatch model, which assumes no scattering, and the diffuse mismatch model, which assumes that all phonons incident on the interface will scatter [90] that can model simple interfaces. However, such models are not applicable to our system due to the complex nature of the interface between the organic and inorganic constituents. Nevertheless, we still expect the observed mismatch in VDOS to cause further scattering of heat carriers which in turn reduces the thermal conductivity of the material below the amorphous limit [5,91]. This is similar to thermal control in self-assembled monolayer junctions, where increasing vibrational mismatch in their metal leads to decreased thermal conduction [92].

Moreover, in Fig. 11c, the observed mismatch between pure polymer and portlandite is more pronounced than the mismatch between pure polymer and tobermorite. Since the inorganic structures in our hybrid systems are portlandite-like (based on XRD results), we expect further reduction of thermal conductivity compared to hybrids of tobermorite.

Next, we look at individual vibrational modes by computing eigenvectors of the dynamical matrix (Eq. (9)). First, locons are distinguished by computing the participation ratio for each mode. In this work, we categorize modes with a participation ratio <0.05 as locons, which is a

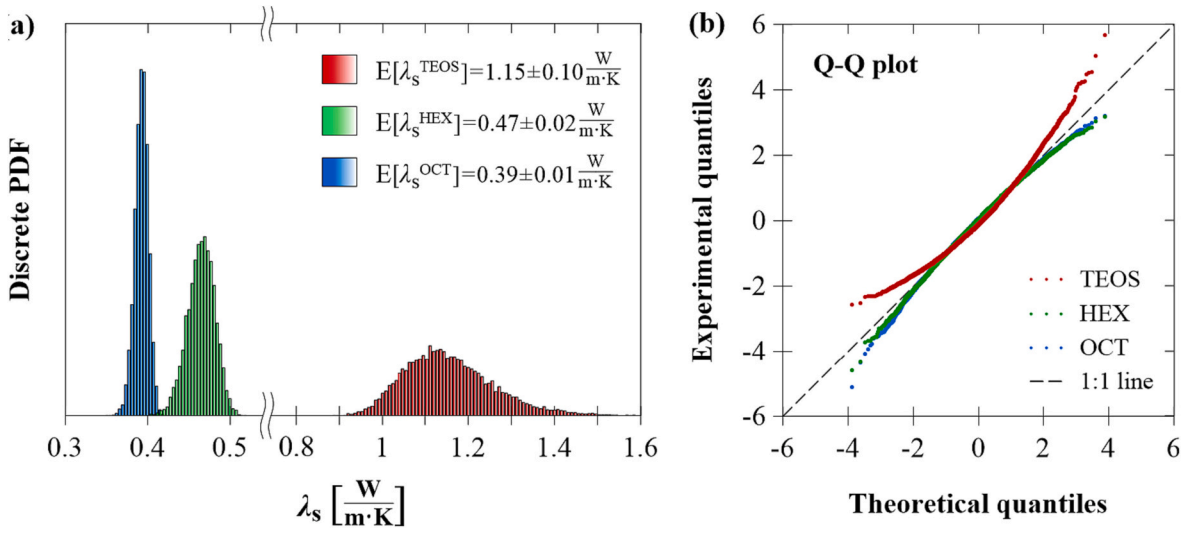

Fig. 10. Discrete probability distributions of the intrinsic thermal conductivity of the reference (TEOS) and cross-linked (HEX and OCT) C-S-H obtained with S—C approximation and Monte-Carlo uncertainty quantification analysis (a). The quantile-quantile (Q-Q) plots associated with each distribution (b).

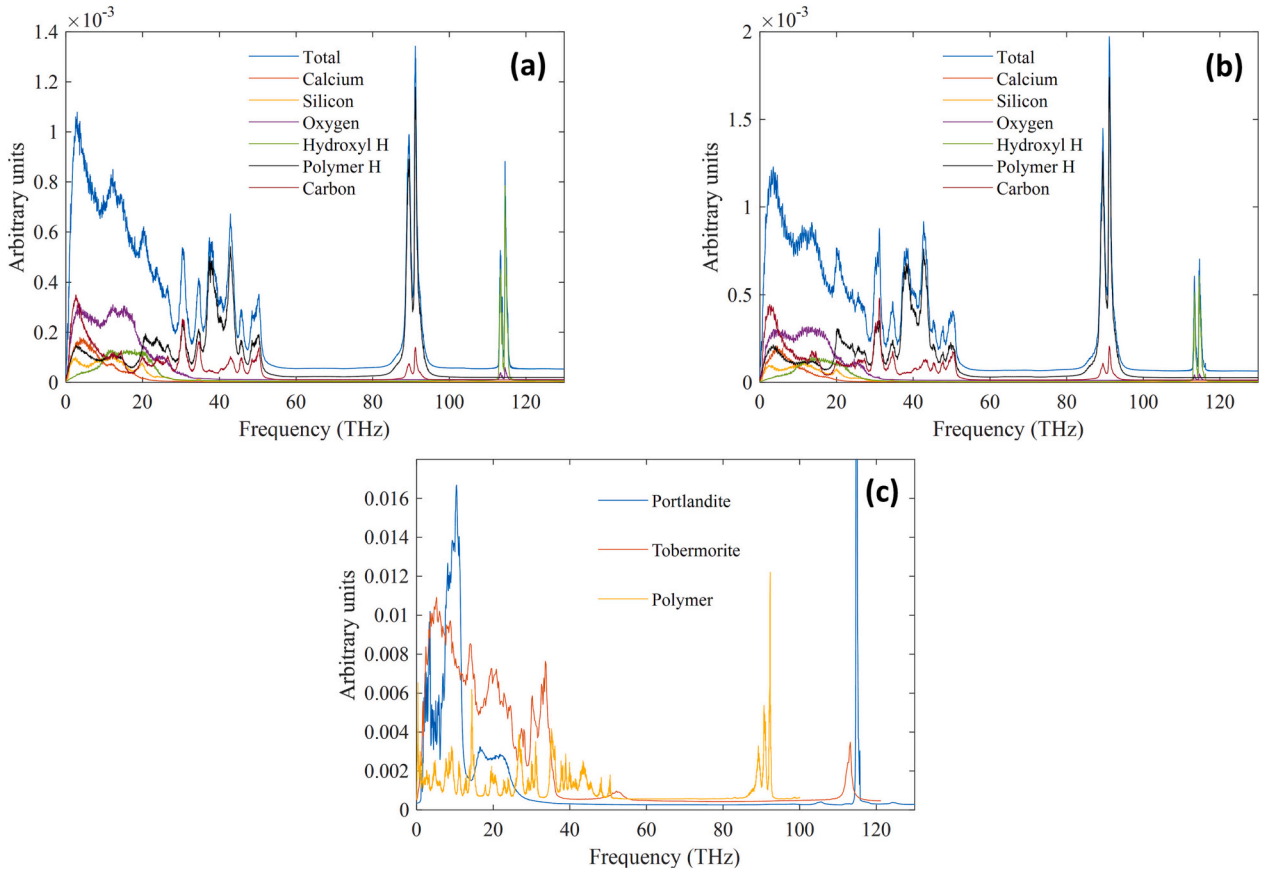

Fig. 11. Vibrational densities of states for (a) cross-linked HEX (b) cross-linked OCT and (c) crystalline portlandite and tobermorite and pure polymer (hexane). The partial VDOS for carbon and hydrogen in polymer provides a region from 35 THz ~ 50 THz, which is absent from the VDOS for portlandite atoms.

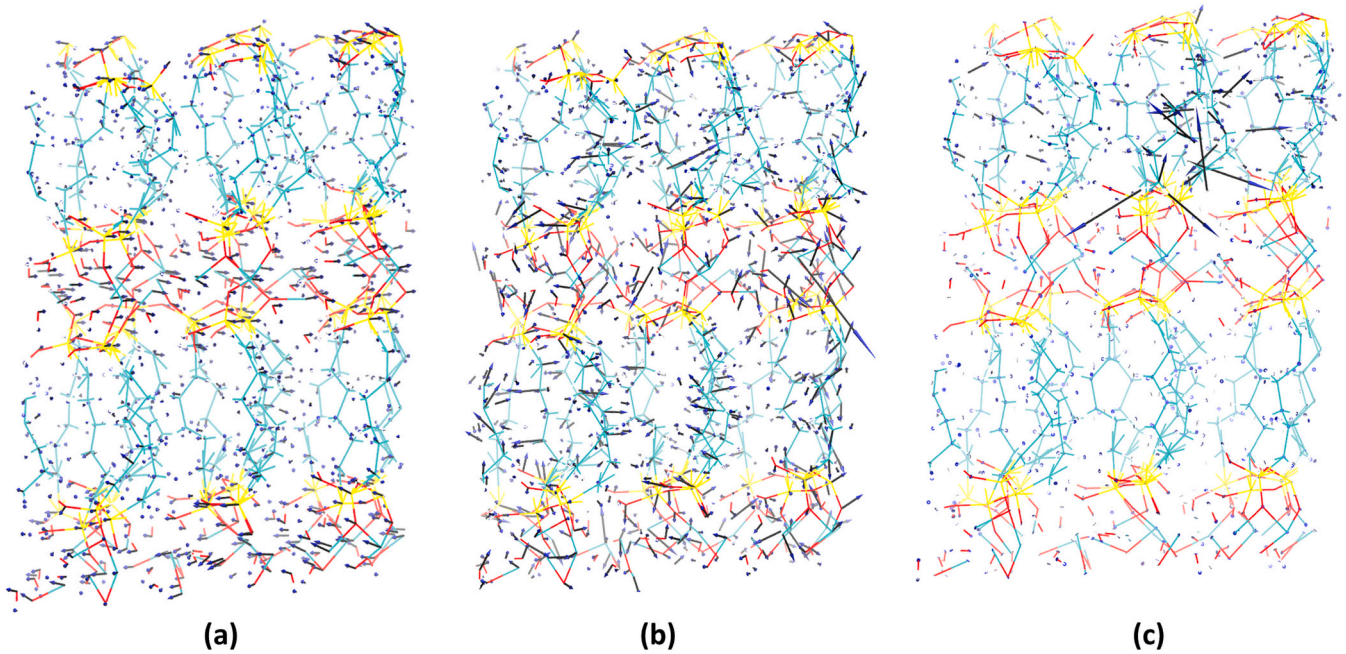

Fig. 12. Visualization of vibrational modes for HEX. The arrows show the mode vectors on each atom. (a) A semi-periodic pattern emerges, which is characteristic of a propagon at lower frequencies. (b) A diffusive mode with the extended but random distribution of mode vectors. (c) A locon with a localized distribution of mode vectors.

more conservative criterion compared to the literature [93]. Propagons are characterized using the 3D Fourier transform of the mode and the z-score described in the Materials and methods section (Eqs. (11) and (12)). Propagons show a wave-like distribution of the mode vectors on atoms. A typical propagating mode is shown in Fig. 12a. Modes that are neither a locon nor a propagon are naturally categorized as a diffuson. The mode vectors for diffusons are randomly distributed over the atoms and don't show any wave-like character. A typical propagating mode is shown in Fig. 12b. This can be contrasted with the mode vectors in locons localized over only a few atoms, as seen in Fig. 12c.

The decomposition of the full spectrum of vibrational modes for HEX: C-S-H and OCT: C-S-H is compared with the results for the tobermorite from our previous work on hybrid systems in Fig. 13 [4]. We observe a significant decrease in the fractional contribution of propagating modes for HEX and OCT compared to the tobermorite. This is expected since the tobermorite has a crystalline structure. However, the percentage of propagating modes is almost unchanged when comparing HEX: C-S-H and OCT: C-S-H. This agrees with our previous work on hybrid structures of tobermorite [4]. However, it is interesting to note the increase in the number of localized modes for OCT: C-S-H compared to the HEX: C-S-H. It is known that localized modes do not carry heat [94]. Hence, we may expect a reduced conductivity in OCT based on this analysis.

The mode categorization indicates that the reduction in thermal conductivity can be attributed partly to fewer propagating modes compared to the crystalline inorganic minerals. Next, we can quantify the diffusive and propagating contributions. The diffusive contribution (λ_d) can be calculated using Allen-Feldman theory (Eq. (6)), and the propagating part of thermal conductivity equals $\lambda_p = \lambda_{GK} - \lambda_d$. As shown in Fig. 14, cross-linking reduces both propagating and diffusive parts in OCT: C-S-H and HEX: C-S-H compared to conventional C-S-H. Furthermore, this reduction positively correlates with the molecular weight or the alkyl chain's length of the organic insert.

In previous work on similar hybrid systems based on tobermorite, only a reduction in the diffusive contribution was observed, which can be attributed to phonon scattering arising from the vibrational mismatch between the organic and inorganic constituents [4]. However, for realistic models constructed from portlandite in this paper, we also observe a reduction in propagating contribution. This points to an additional mechanism present in portlandite layers as compared to tobermorite layers. A possible contributor could be the varying distortion of polymers in HEX: C-S-H and OCT: C-S-H. However, our calculations show that the average silicon-to-silicon distance in both atomistic models is comparable to the fully stretched polymer length, which is 94 % and 95 % for HEX and OCT: C-S-H, respectively. The stretched conformation state of the alkyl chain is corroborated by the experimentally measured interlayer distance, Fig. 2 [29], which strongly indicates the organics monolayer in both structures. Such a small difference suggests that a more disordered organic layer in the OCT: C-S-H cannot be at the origin of its reduced thermal conductivity compared to HEX: C-S-H. Besides the organic layer, a more disordered CaO layer can also cause a reduction in the propagative heat conduction contribution by disrupting the phonon transport. Such a disorder might explain the observed decrease in propagative contributions.

To gain more insight into the disorder in portlandite layers, the out-of-plane distortion of intralayer calcium atoms about their mean value is considered (Fig. 15). We observe a broadening of the distribution for OCT: C-S-H when compared to HEX: C-S-H. The FWHM increases from 0.90 Å in the HEX case to 1.19 Å for OCT: C-S-H, which confirms our hypothesis that Ca—O layers become more disordered as the length of the organic molecule increases.

4. Discussion

4.1.1. C-S-H and the minimum thermal conductivity λ_{min}

It is commonly accepted that the C-S-H molecular structure is that of a defective crystal analog, 11 Å tobermorite [74–76,78,95,96]. For example, C-S-H successive layers experience random translations in the **a-b** crystal plane and/or rotations about the normal, both typical for disordered crystals with the turbostratic disorder [97]. Additionally, the structure contains vacancy-type defects in its dreierkette silicate chains. As a result, the X-ray diffraction spectra of C-S-H exhibit only a few broad and asymmetric peaks (Fig. 2a), suggesting limited long-range order and semi-amorphous nature. Given the highly disordered C-S-H structure, the estimation of the *minimum thermal conductivity* [5,98] of C-S-H might be attempted and compared with the experimental and MD-based values reported in this and our previous works [2–4].

According to Cahill [5,98] the disorder lowers thermal conductivity in crystals, and the lowest achievable thermal conductivity corresponds to disordered crystals in which phonon transport characteristics are that of phonon transport in glasses. The thermal conductivity of amorphous solids above ~50 K, $\lambda_{am} = \lambda_{min}$, can be described by the modified Einstein's model [5], in which the heat transport results from the random walk of the thermal energy between localized quantum mechanical oscillators, Eq. (18):

$$\lambda_{am} = \left(\frac{\pi}{6}\right)^{\frac{1}{3}} k_B n^{\frac{2}{3}} \sum_i v_i \left(\frac{T}{\theta_i}\right)^2 \int_0^{\frac{\theta_i}{T}} \frac{x^3 e^x}{(e^x - 1)^2} dx \tag{18}$$

In Eq. (18), the sum is taken over three sound velocities, v_i (two transversal and one longitudinal), T is the temperature, and θ_i is a cutoff frequency expressed by Eq. (19):

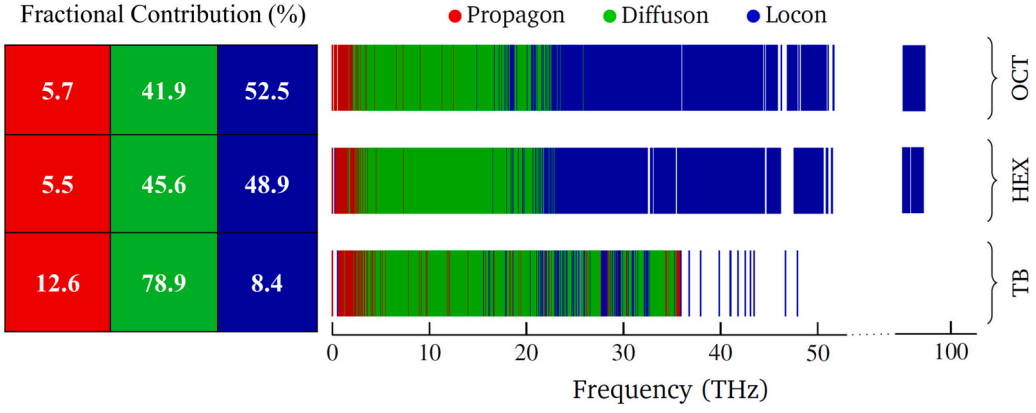

Fig. 13. Spectral analysis of vibrational modes for Tobermorite (TB), HEX: C-S-H and OCT: C-S-H. The percentage of propagating modes is almost unchanged between HEX and OCT. In contrast, the percentage of localized modes increases with the molecular weight - organosilane cross-linking molecule or the chain length.

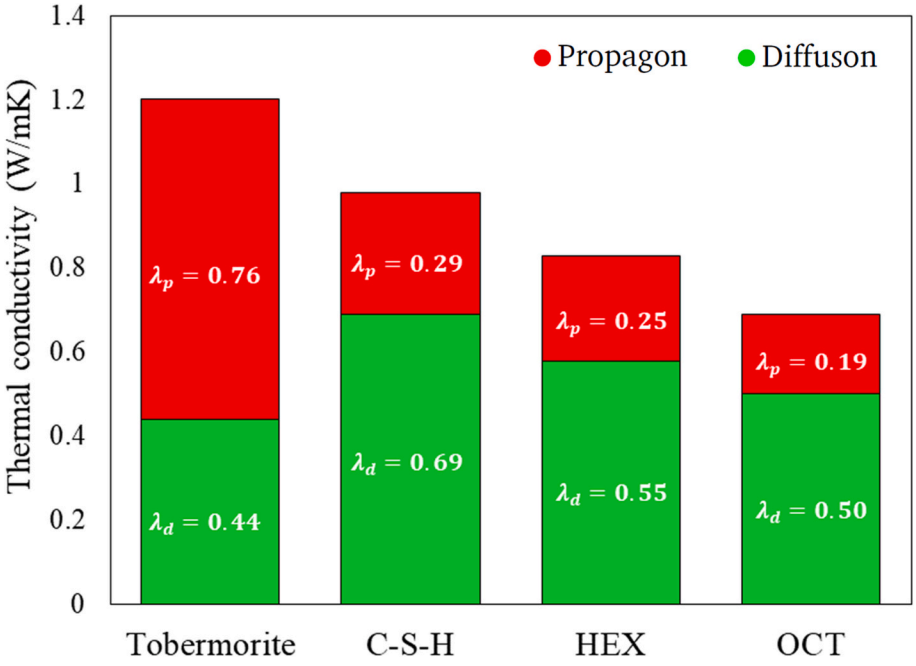

Fig. 14. The contributions of propagative (λ_p) and diffusive (λ_d) modes to the total thermal conductivity of 11 Å tobermorite (Ca/Si = 1), the classical (Ca/Si = 1.75), and cross-linked HEX and OCT: C-S-H. C-S-H values adapted from Zhou et al. [3].

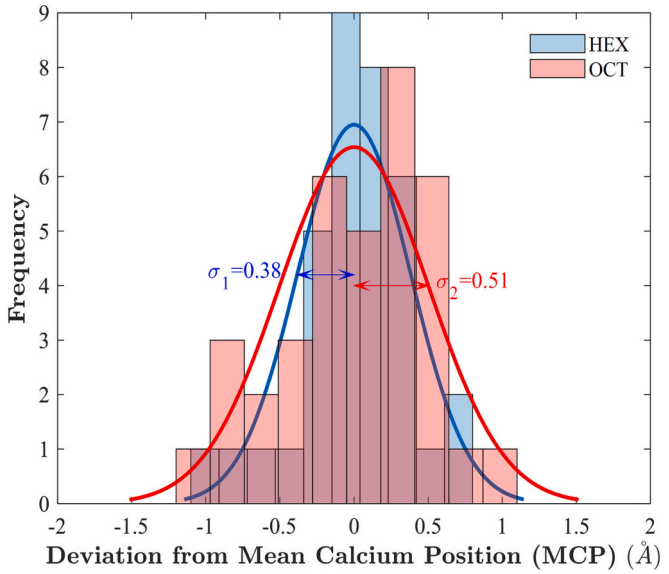

Fig. 15. Deviation of calcium atoms from the mean position within the CaO layer. The Gaussian fits to the data show a significant increase in standard deviation with increasing chain length. This points to an increased disorder in crystalline calcium layers.

$$\theta_i = \upsilon_i \left(\frac{\hbar}{k_B}\right)\left(6\pi^2 n\right)^{\frac{1}{3}} \tag{19}$$

where $\hbar$ is the reduced Planck constant, k_B is Boltzmann constant, and n stands for the number density of atoms.

Table 3 presents the estimates of the λ_{am} for selected solids, including high and low calcium C-S-H, as well as an example of C-A-S-H. When possible, the quasi-isotropic longitudinal, υ_l, and transversal, υ_t, sound velocities are calculated from the average principal sound velocities $c_1 > c_2 > c_3$ [99]. Otherwise, they are estimated from the usual relation between bulk, shear modulus, and solid density [99]. Both moduli are considered in the Voight-Reuss-Hill sense. The application of the modified Einstein's model, Eq. (18), estimates the amorphous limit of ≈1.1 to 1.2 $Wm^{-1}K^{-1}$ for C-S-H. This limit tends to be valid irrespective of the Ca/Si ratio. This trend is consistent with Qomi et al.'s [2] original observation, who demonstrated a statistically similar volumetric conductivity for the first time for low and high lime C-S-H. Therefore, the simple stoichiometric modifications to C-S-H molecular structure relying solely on the Ca/Si modulation, e.g., the introduction of SiO_4-ion through the use of reactive silica via pozzolanic reaction, does not alter the overall picture of nanoscale thermal energy transport. Although the density of vacancies (defects) in C-S-H increases with the Ca/Si ratio leading to a higher degree of disorder, the literature suggests that such an increase is very modest in the $Ca/Si \in (1.0; 2.0)$ range [75,100]. On the other hand, studies on the C-S-H's molecular level suggest the heat transport in diffusive regime [2], thus effectively diminishing the phonon-vacancy scattering effects. Moreover, we observe a close alignment of the experimentally determined conductivity, see Figs. 9 and 10a, with the amorphous limit reported in Table 3. This strongly suggests that despite the existence of some degree of the long-range order, the glass-like heat energy transport model tends to be applicable to capture C-S-H's volume average thermal conductivity.

Given the ineffectiveness of Ca/Si modulation in reducing the thermal conductivity of C-S-H, a brief consideration is given to the effect of C-S-H dopping with aluminum. This element is commonly associated with the Al-rich supplementary cementitious materials [1], which are used as partial cement replacement in concrete, and its hydration results in calcium-aluminate-silicate-hydrate, C-A-S-H. The substitution of Si^{4+} by Al^{3+} in the C-A-S-H structure most often happens at bridging sites of the dreierketten chain [67,100,104], and under certain thermodynamic conditions, it may result in the cross-linking [104,105]. Table 3 reports the amorphous thermal conductivity limit calculated for C-A-S-H reported by Geng et al. [101]. For these particular calculations, three variants are considered in terms of C-A-S-H density, which is not reported in [101]. In all cases, our calculations indicate the amorphous limit slightly above the one calculated for Al-free C-S-H. However, these results should be interpreted in the semi-quantitative sense due to the lack of uncertainty in the reported estimates. Despite this drawback, this analysis still indicates the ineffectiveness of the Al-doping of C-S-H in

Table 3
Calculated amorphous limit thermal conductivities for selected C-S-H and C-A-S-H solids.

C-(A)-S-H	Sound velocities						ρ (g/cm^3)	λ_{am} (Wm^{-1} K^{-1})	Ref.
	n (10^{22} cm^{-3})	c_1	c_2	c_3	v_l	v_t[c]			
$C_{1.65}$-S-$H_{1.75}$	9.67	5.61	3.21	2.77	5.61	2.99[a]	2.56	1.16	[99]
$C_{1.64}$-S-$H_{1.39}$	8.39	–	–	–	6.29	3.17	2.36	1.13	[3]
		–	–	–	6.01	3.22			
$C_{1.75}$-S-$H_{2.0}$	9.30	–	–	–	4.79	3.25	2.40	1.14	[2]
$C_{1.0}$-S-$H_{0.5}$	7.97	–	–	–	5.16	3.75	2.55		
	8.94	–	–	–	5.02	3.76	2.52[b]	1.21	
		6.68	3.96	3.59	6.68	3.77		1.28	
$C_{1.0}$-$A_{0.1}$-S-H	9.68	–	–	–	4.82	3.61	2.73[b]	1.23	[101]
		6.42	3.80	3.45	6.42	3.63		1.31	
	10.0	–	–	–	4.74	3.55	2.83[b]	1.24	
		6.31	3.73	3.39	6.31	3.56		1.32	

$c_{1,2,3}$, longitudinal and transversal velocities in km/s collected from listed references.
[a] $v_t = (c_{1+}\ c_2)\ /\ 2$.
[b] Lower density limit corresponding to hydrogarnet, middle and higher density limit representing siliceous hydrogarnet, density values after [100,102,103].
[c] When $c_{1,2,3}$ not specified longitudinal and transversal sound velocities calculated from Voight-Reuss-Hill bulk and shear moduli calculated from the full stiffness tensor.

lowering its intrinsic thermal conductivity.

4.1.2. The convergence of experiment and atomistic simulations

Our work's experimental and atomistic analysis results reveal a significant reduction in the intrinsic thermal conductivity of cross-linked C-S-H gel benchmarked against inorganic C-S-H (Ca/Si = 1). In this aspect, both approaches deliver a qualitative agreement. However, we observe a discrepancy between both methods on a quantitative basis, with the MD-based estimates systematically higher than the experimental ones, Figs. 10a and 14. Several phenomena may lead to such a difference, one of them being the size and texture (defects) of the material domain through which the heat transport is considered in each case. In MD, we operate at the scale of the unit cell, while the experimentally derived S—C estimates consider the nanoscale particle as a crystallite [106].

To demonstrate the relevance and validity of both estimates, we build the series resistance model, Eq. (20), in which the total thermal resistance of the cross-linked C-S-H nanolaminate particle is the sum of each layer and the interfacial resistance.

$$\frac{L}{\lambda_{eff}} = \sum \frac{l_i}{\lambda_i} + \sum \frac{1}{G_i} \tag{20}$$

Here, L is the effective particle size in the direction of the heat flow, l_i is the thickness of each layer, λ_i is the conductivity of each layer, λ_{eff} is the effective conductivity of the nanolaminate particle, and G_i stands for interfacial conductance [4,10]. For the sake of the argument, in the first-order approximation, we assume no interfacial effect by neglecting the second term in Eq. (20). Therefore, the effective conductivity is the function of the number of unit cells in the crystallite, n, basal spacing, d, the unit cell conductivity, λ_v (obtained from MD-simulations), and the conductivity of organosilanes, λ_O, which condense on the particle's surface creating an adsorbed layer of average thickness $\tilde{l}$, Eq. (21).

$$\lambda_{eff} = \frac{(nd + 2\tilde{l})\lambda_v\lambda_O}{nd\lambda_O + 2\tilde{l}\lambda_v} \tag{21}$$

We use the Scherrer equation [107] to estimate the "apparent size" (employing the integral breadth, β, of the basal reflection in cross-linked C-S-H measured through XRD and reported in [29]) and the number of unit cells which define the crystallite, Table 4. Additionally, the lack of reliable data on the intrinsic thermal conductivity of bis-organosilanes and the knowledge of the conformational state of organic molecules in the adsorbed layer, and the grafting density, is mitigated by considering the approximate range of λ_O. This range is defined by the thermal properties of amorphous organics: dodecane (lower bound) and polymethyl methacrylate (upper bound) [10]. Also, it encompasses available experimental conductivities measured on selected species from silanes and siloxane families [108].

Table 4
Comparison of series-resistance estimate vs. measured effective thermal conductivity of cross-linked C-S-H crystallites.

Solid	Input parameters						λ_{eff}[b]	λ_{S-C}[b]
	β (°2θ)	d (Å)	n[c]	$\tilde{l}$ (Å)	λ_v[b]	λ_O[b]		
HEX: C-S-H	1.58	14.05	4	9.30	0.83 ± 0.05	0.14[a] 0.20[a]	0.37 0.47	0.46 ± 0.02
OCT: C-S-H	1.48	16.18	4	11.78	0.69 ± 0.05	0.14 0.20	0.34 0.42	0.39 ± 0.01

[a] Lower and upper bound values correspond to liquid dodecane = 0.14 Wm^{-1} K^{-1} and an amorphous polymethyl methacrylate = 0.20 Wm^{-1} K^{-1}, after the Ref [10].
[b] Thermal conductivity expressed in Wm^{-1} K^{-1}.
[c] Expressed as the closest integer value.

Although the series-resistance model represents a quite simplistic view, we observe, at the particle scale of cross-linked C-S-H nanolaminate, the thermal conductivity is substantially below its intrinsic value estimated via the MD approach at the scale of the unit cell, Table 4. Moreover, such a reduction is driven by the organics layer condensed on the nanocrystallite surface, which acts as an additional thermal resistance constraining the heat conduction through the particle domain. The alignment of the experimentally obtained self-consistent estimate of conductivity, λ_{S-C}, with the calculated bounds, corroborates such a mechanism.

4.1.3. Statistical testing of postulated hypothesis

In Fig. 10a, we presented experiment-based discrete probability distributions of thermal conductivity for reference C-S-H and its cross-linked variants. It is apparent the differences between expected values: (1) $E[\lambda_s^{TEOS}] - E[\lambda_s^{HEX}]$ and (2) $E[\lambda_s^{TEOS}] - E[\lambda_s^{OCT}]$, are much larger than each case's combined uncertainty in thermal conductivities. Moreover, the two-sample t-test [109] with unequal variances rejects the null hypothesis $H_0 : E[\lambda_s^{TEOS}] - E[\lambda_s^{HEX,OCT}] = 0$ at the significance level $\alpha = 0.05$ in favor of $H_1 : E[\lambda_s^{TEOS}] - E[\lambda_s^{HEX,OCT}] \rangle 0$ at $p - value \ll \alpha$. Likewise, statistical testing of the MD-based estimates leads to the same outcome. It is noted that the experiment and MD simulations reveal a slight divergence of conductivity distribution from normality, Fig. 10b. However, the large sample size used in both methods, $N \geq 10,000$, allows us to apply a t-test to non-Gaussian populations by using the Central Limit Theorem [109]. The current analysis supports the postulated hypothesis: "The cross-linking with functionalized organosilane molecules decreases conductive heat transport in C-S-H nanolaminates."

5. Summary and conclusions

This work concerned determining the effect of organic cross-linking on the thermal conductivity of C-S-H at the nanoscale. By referring to the presented suite of experimental, analytical, and atomistic modeling methods, we were able to test the validity of the postulated hypothesis. Such a hypothesis-testing approach allows us to draw the following primary conclusions.

First, the molecular scale cross-linking of calcium silicate hydrates with bis-organosilanes effectively reduces its thermal conductivity at the nanoscale. This fact draws its support from the analytical inference of the intrinsic conductivity of modified solids based on the effective conductivity measurements collected in the steady-state heat flow experiments. At the nano-crystallite particle scale, the observed reduction in cross-linked gels amounts approximately to 60 % (CH_2 chain of 6) and 70 % (CH_2 chain of 8) of the conductivity observed for classical C-S-H (Ca/Si = 1, 1.15 $Wm^{-1} K^{-1}$). The atomistic simulations corroborate this fact by independently revealing the significantly lower conductivities at the unit cell scale of cross-linked C-S-H as compared to inorganic C-S-H as well as its crystalline archetype 11 Å tobermorite. Through the detailed study of heat transport at the molecular level, we show that C-S-H cross-linking promotes localized phonons (locons) on the expense of propagating (propagons) and diffusive (diffuson) modes. Such redistribution of vibrational modes is at the core of thermal conductivity reduction in hybridized C-S-H solids. In both methods, observed differences are statistically significant.

Second, the decrease in the intrinsic thermal conductivity of cross-linked C-S-H correlates with the molecular weight of the bis-organosilane agent or otherwise said with its CH_2 linear chain length. Based on the presented evidence, such a positive correlation partially derives from the apparent density reduction; gels cross-linked with longer chain organosilane molecules display larger interlayer spacing. Additionally, by increasing the alkyl chain length, we enhance the participation ratio of locons and amplify the molecular disordered in intralayer calcium atoms.

Third, the thermal conductivity of inorganic C-S-H (Ca/Si = 1) corresponds to the conductivity of disordered crystals in which heat transport characteristics are that of phonons in glasses. This conclusion arrives from the close match between the experimentally inferred conductivity and the amorphous limit calculated with the modified Einstein's model. It is also aligned with the results of an independent atomistic study by Qomi et al. [2], who demonstrated statistically similar volumetric conductivity for low and high lime C-S-H.

Fourth, a developed realistic atomistic model, constructed on the portlandite molecular framework, provides reliable insight into the heat transport mechanism in cross-linked C-S-H. This original model offers a qualitative thermal conductivity prediction at the unit cell scale, which is compatible with experimentally determined values at the nano-crystallite particle level. The observed quantitative difference can be explained by the size and texture effects of the material domain through which the heat transport is considered in experimental analysis and atomistic simulations. Finally, the developed model agrees well with the experimentally determined apparent densities of hybridized C-S-H solids.

CRediT authorship contribution statement

Amir Moshiri: Investigation, Formal analysis, Validation, Methodology, Writing – original draft, Writing – review & editing. **Ali Morshedifard:** Software, Formal analysis, Validation, Methodology, Writing – original draft, Writing – review & editing. **Damian Stefaniuk:** Investigation, Software, Formal analysis, Validation, Writing – original draft, Writing – review & editing. **Santiago El Awad:** Investigation, Validation, Writing – review & editing. **Tejasree Phatak:** Investigation, Methodology, Writing – review & editing. **Kamil J. Krzywiński:** Validation, Writing – review & editing. **Debora Frigi Rodrigues:** Funding acquisition, Resources, Writing – review & editing. **Mohammad Javad Abdolhosseini Qomi:** Conceptualization, Writing – original draft, Writing – review & editing, Funding acquisition, Formal analysis, Methodology, Project administration, Resources, Supervision. **Konrad J. Krakowiak:** Conceptualization, Writing – original draft, Writing – review & editing, Funding acquisition, Formal analysis, Methodology, Project administration, Resources, Supervision.

Declaration of competing interest

The authors declare that they have no known competing financial interests or personal relationships that could have appeared to influence the work reported in this paper.

Data availability

Data will be made available on request.

Acknowledgment

The National Science Foundation supported this work under Grants No. 1825921, 1826122, and The Welch Foundation award No. E-2011-20190330. Mr. Santiago El Awad would like to acknowledge the additional support provided by the Anton Paar USA, Inc. and the Dwight David Eisenhower Transportation Fellowship Program (DDETFP) from U.S. Department of Transportation, Federal Highway Administration, award number 693JJ32145075 and 693JJ32245048. Mr. Kamil J. Krzywiński is grateful to the NAWA Polish National Agency for Academic Exchange for financial support through Academic Exchange NAWA Preludium Bis 1 program No. PPN/STA/2021/1/00012 which is a part of Grants No. 2019/35/O/ST8/01546 supported by National Science Centre (Poland).

Appendix A. Supplementary data

Supplementary data to this article can be found online at https://doi.org/10.1016/j.cemconres.2023.107324.

References

[1] S. Mindess, J.F. Young, D. Darwin, Concrete, second ed., Prentice Hall, 2002.
[2] M.J.A. Qomi, F.J. Ulm, R.J.M. Pellenq, Physical origins of thermal properties of cement paste, Phys. Rev. Appl. 3 (6) (2015), 064010, https://doi.org/10.1103/PhysRevApplied.3.064010.
[3] Y. Zhou, A. Morshedifard, J. Lee, M.J.A. Qomi, The contribution of propagons and diffusons in heat transport through calcium-silicate-hydrates, Appl. Phys. Lett. 110 (2017), 043104, https://doi.org/10.1063/1.4975159.
[4] A. Morshedifard, A. Moshiri, K.J. Krakowiak, M.J.A. Qomi, Spectral attributes of sub-amorphous thermal conductivity in cross-linked organic–inorganic hybrids, Nanoscale 12 (2020) 13491–13500, https://doi.org/10.1039/D0NR02657C.
[5] D.G. Cahill, S.K. Watson, R.O. Pohl, Lower limit to the thermal conductivity of disordered crystals, Phys. Rev. B 46 (1992) 6131, https://doi.org/10.1103/PhysRevB.46.6131.
[6] R.J.M. Pellenq, N. Lequex, H. van Damme, Engineering the bonding scheme in C-S-H: the iono-covalent framework, Cem. Concr. Res. 38 (2) (2008) 159–174, https://doi.org/10.1016/j.cemconres.2007.09.026.
[7] C. Plassard, E. Lesniewska, I. Pochard, A. Nonat, Nanoscale experimental investigation of particle interactions at the origin of the cohesion of cement, Langmuir. 21 (2005) 7263–7270, https://doi.org/10.1021/la050440+.
[8] J.E. Parrott, A.D. Stuckes, Thermal Conductivity of Solids, Pion, London, 1975.
[9] M. Beekman, D.G. Cahill, Inorganic crystals with glass-like and ultralow thermal conductivities, Cryst. Res. Technol. 52 (2017), 1700114, https://doi.org/10.1002/crat.201700114.
[10] M.D. Losego, I.P. Blitz, R.A. Vaia, D.G. Cahill, P.V. Braun, Ultralow thermal conductivity in organoclay nanolaminates synthesized via simple self-assembly, Nano Lett. 13 (5) (2013) 2215–2219, https://doi.org/10.1021/nl4007326.
[11] J. Liu, B. Yoon, E. Kuhlmann, M. Tian, J. Zhu, S.M. George, Y.C. Lee, R. Yang, Ultralow thermal conductivity of atomic/molecular layer-deposited hybrid organic-inorganic zircone thin films, Nano Lett. 13 (2013) 5594–5599, https://doi.org/10.1021/nl403244s.
[12] X. Qian, X. Gu, R. Yang, Thermal conductivity modelling of hybrid organic-inorganic crystals and superlattices, Nano Energy 41 (2017) 394–407, https://doi.org/10.1016/j.nanoen.2017.09.047.

[13] H. Matsuyama, J.F. Young, Intercalation of polymers in calcium silicate hydrate: a new synthetic approach to biocomposites? Chem. Mater. 11 (1999) 16–19, https://doi.org/10.1021/cm980549l.

[14] H. Matsuyama, J.F. Young, Synthesis of calcium silicate hydrate/polymer complexes: part I. Anionic and nonionic polymers, J. Mater. Res. 14 (1999) 3379–3388, https://doi.org/10.1557/JMR.1999.0458.

[15] H. Matsuyama, J.F. Young, Synthesis of calcium silicate hydrate/polymer complexes: part II. Cationic polymers and complex formation with different polymers, J. Mater. Res. 14 (1999) 3389–3396, https://doi.org/10.1557/JMR.1999.0459.

[16] S.C. Mojumdar, L. Raki, Preparation and properties of calcium silicate hydrate-poly (vinyl alcohol) nanocomposite materials, J. Therm. Anal. Calorim. 82 (2005) 89–95, https://doi.org/10.1007/s10973-005-0846-8.

[17] F. Merlin, H. Lombois, S. Joly, N. Lequeux, J.L. Halary, H. Van Damme, Cement-polymer and clay-polymer nano- and meso-composites: spotting the difference, J. Mater. Chem. 12 (2002) 3308–3315, https://doi.org/10.1039/B205279M.

[18] F. Pelisser, P.J.P. Gleize, A. Mikowski, Structure and micro-nanomechanical characterization of synthetic calcium-silicate-hydrate with poly(vinyl)alcohol, Cem. Concr. Compos. 48 (2014) 1–8, https://doi.org/10.1016/j.cemconcomp.2014.01.004.

[19] Y. Zhou, C.A. Orozco, E. Duque-Redondo, H. Manzano, G. Geng, P. Feng, P.J.M. Monteiro, C. Miao, Modification of poly(ethylene glycol) on the microstructure and mechanical properties of calcium silicate hydrates, Cem. Concr. Res. 115 (2019) 20–30, https://doi.org/10.1016/j.cemconres.2018.10.001. ISSN 0008-8846.

[20] J.J. Beaudoin, L. Raki, R. Alizadeh, A 29Si MAS NMR study of modified C-S-H nanostructures, Cem. Concr. Compos. 31 (2009) 585–590, https://doi.org/10.1016/j.cemconcomp.2008.11.004.

[21] J.J. Beaudoin, H. Dramé, L. Raki, R. Alizadeh, Formation and properties of C-S-H–PEG nano-structures, Mater. Struct. 42 (2009) 1003–1014, https://doi.org/10.1617/s11527-008-9439-x.

[22] J.J. Beaudoin, H. Dramé, L. Raki, R. Alizadeh, Formation and characterization of calcium silicate hydrate–hexadecyltrimethylammonium nanostructure, J. Mater. Res. 23 (2008) 2804–2815, https://doi.org/10.1557/JMR.2008.0342.

[23] V. Kanchanason, J. Plank, Role of pH on the structure, composition and morphology of CSH–PCE nanocomposites and their effect on early strength development of Portland cement, Cem. Concr. Res. 102 (2017) 90–98, https://doi.org/10.1016/j.cemconres.2017.09.002.

[24] R. Alizadeh, J.J. Beaudoin, L. Raki, V. Terskikh, C-S-H/polyaniline nanocomposites prepared by in-situ polymerization, J. Mater. Sci. 46 (2011) 460–467, https://doi.org/10.1007/s10853-010-4918-1.

[25] A. Popova, G. Geoffroy, M.F. Renou-Gonnord, P. Faucon, E. Gartner, Interactions between polymeric dispersants and calcium silicate hydrates, J. Am. Ceram. Soc. 83 (2000) 2556–2560, https://doi.org/10.1111/j.1151-2916.2000.tb01590.

[26] J. Ha, S. Chae, K.W. Chou, T. Tyliszczak, P.J.M. Monteiro, Effect of polymers on the nanostructure and on the carbonation of calcium silicate hydrates: a scanning transmission X-ray microscopy study, J. Mater. Sci. 47 (2012) 976–989, https://doi.org/10.1007/s10853-011-5877-x.

[27] R. Khoshnazar, J.J. Beaudoin, L. Raki, A. Alizadeh, Characteristics and engineering performance of C-S-H/Aminobenzoic acid composite systems, J. Adv. Concr. Technol. 13 (2015) 415–420, https://doi.org/10.3151/jact.13.415.

[28] F. Pelisser, P.J.P. Gleize, A. Mikowski, Effect of poly(diallyldimethylammonium chloride) on nanostructure and mechanical properties of calcium silicate hydrate, Mater. Sci. Eng. A 527 (2010) 7045–7049, https://doi.org/10.1016/j.msea.2010.07.057.

[29] A. Moshiri, D. Stefaniuk, S.K. Smith, A. Morshedifard, D. Frigi Rodrigues, M.J. A. Qomi, K.J. Krakowiak, Structure and morphology of calcium-silicate-hydrates cross-linked with dipodal organosilanes, Cem. Concr. Res. 133 (2020), 106076, https://doi.org/10.1016/j.cemconres.2020.106076.

[30] A. Javadi, T. Jamil, E. Abouzari-Loft, M.D. Soucek, H. Heinz, Working mechanisms and design principles of comb-like polycarboxylate ether superplasticizers in cement hydration: quantitative insights for a series of well-defined copolymers, ASC Sustain. Chem. Eng. 9 (2021) 8354–8371, https://doi.org/10.1021/ascsuschemeng.0c08566.

[31] A. Picker, L. Nicoleau, Z. Burghart, J. Bill, I. Zlotnikov, C. Lebbez, A. Nonat, H. Cölfen, Mesocrystaline calcium silcate hydrate: a bioinspired route toward elastic concrete materials, Sci. Adv. 3 (2017) 11, https://doi.org/10.1126/sciadv.1701216.

[32] A. Picker, Influence of Polymers on Nucleation and Assembly of Calcium Silicate Hydrates, Ph.D. Thesis,, Universität Konstanz, 2013.

[33] K.S. Katti, D.R. Katti, Why is nacre so tough and strong? Mater. Sci. Eng. C 26 (8) (2006) 1317–1324, https://doi.org/10.1016/j.msec.2005.08.013.

[34] A.P. Jackson, J.F. Vincent, R.M. Turner, The mechanical design of nacre, Proc. R. Soc. Lond. B 234 (1277) (1988) 415–440, https://doi.org/10.1098/rspb.1988.0056.

[35] Y. Zhou, D. Hou, H. Manzano, C.A. Orozco, G. Geng, P.J.M. Monteiro, J. Liu, Interfacial connection mechanisms in calcium-silicate-hydrates/polymer nanocomposites: a molecular dynamics study, Appl. Mater. Interfaces 9 (2017) 41014–41025, https://doi.org/10.1021/acsami.7b12795.

[36] Y. Zhou, L. Tang, J. Liu, Ch. Miao, Interaction mechanisms between organic and inorganic phases in calcium silicate hydrates/poly(vinyl alcohol) composites, Cem. Concr. Res. 125 (2019), 105891, https://doi.org/10.1016/j.cemconres.2019.105891.

[37] L. Ukrainczyk, R.A. Bellman, A.B. Anderson, Template synthesis and characterization of layered Al- and Mg-silsesquioxanes, J. Phys. Chem. B 101 (1997) 531–539, https://doi.org/10.1021/jp962937l.

[38] J. Minet, S. Abramson, B. Bresson, C. Sanchez, V. Montouillot, N. Lequeux, New layered calcium organosilicate hybrids with covalently linked organic functionalities, Chem. Mater. 16 (2004) 3955–3962, https://doi.org/10.1021/cm034967o.

[39] J. Minet, S. Abramson, B. Bresson, A. Franceschini, H. Van Damme, N. Lequeux, Organic calcium silicate hydrate hybrids: a new approach to cement based nanocomposites, J. Mater. Chem. 16 (2006) 1379–1383, https://doi.org/10.1039/B515947D.

[40] A. Franceschini, S. Abramson, V. Mancini, B. Bresson, Ch. Chassenieux, N. Lequeux, New covalent bonded polymer–calcium silicate hydrate composites, J. Mater. Chem. 17 (2007) 913–922, https://doi.org/10.1039/B613077A.

[41] A. Buryachanko, Micromechanics of Heterogeneous Materials, Springer, 2007.

[42] P.B. Allen, J.L. Feldman, Thermal conductivity of disordered harmonic solids, Phys. Rev. B 48 (1993) 12581, https://doi.org/10.1103/PhysRevB.48.12581.

[43] K.J. Krakowiak, R.G. Nannapaneni, A. Moshiri, T. Phatak, D. Stefaniuk, L. Sadowski, M.J.A. Qomi, Engineering of high specific strength and low thermal conductivity cementitious composites with hollow glass microspheres for high-temperature high-pressure applications, Cem. Concr. Compos. 108 (2020), 103514, https://doi.org/10.1016/j.cemconcomp.2020.103514.

[44] ASTM C518-04, Standard Test Method for Steady-state Thermal Transmission Properties by Means of the Heat Flow Meter Apparatus, American Society for Testing and Materials, 2004.

[45] ASTM E 1530-06, Standard Test Method for Evaluating the Resistance to Thermal Transmission of Materials by the Guarded Heat Flow Meter Technique, American Society for Testing and Materials, 2006.

[46] A. Brzezinski, A. Tleoubaev, Effects of interface resistance on measurements of thermal conductivity of composites and polymers, in: Proceedings of the 30th Annual Conference on Thermal Analysis and Applications, Pittsburgh, PA, USA, 2002.

[47] A. Tleoubaev, Use of Heat Flow Meter Instruments for Testing Thin and Thick Samples, ASTM Meeting, Houston, TX, USA, 2019.

[48] S. Nemat-Nasser, M. Hori, Micromechanics: Overall Properties of Heterogeneous Materials, second ed., North-Holland, 1999.

[49] K. Kadoya, N. Matsunaga, A. Nagashima, Viscosity and thermal conductivity of dry air in the gaseous phase, J. Phys. Chem. Ref. Data Monogr. 14 (4) (1985) 947–970, https://doi.org/10.1063/1.555744.

[50] J.D. Eshelby, The determination of the elastic field of an ellipsoidal inclusion and related problems, Proc. R. Soc. Lond. A 241 (1957) 376–396, https://doi.org/10.1098/rspa.1957.0133.

[51] D. Łydżba, A. Różański, D. Stefaniuk, Equivalent microstructure problem: mathematical formulation and numerical solution, Int. J. Eng. Sci. 123 (2018) 20–35, https://doi.org/10.1016/j.ijengsci.2017.11.007.

[52] P.R. Bevington, D.K. Robinson, Data Reduction and Error Analysis for the Physical Sciences, third ed., McGraw-Hill, 2002.

[53] D.M. Henderson, H.S. Gutowsky, A nuclear magnetic resonance determination of the hydrogen positions in $Ca(OH)_2$, Am. Mineral. 47 (11–12) (1962) 1231–1251.

[54] R.G. Parr, W. Yang, Density-Functional Theory of Atoms and Molecules, Oxford University Press, New York, 1989.

[55] G. Kresse, J. Hafner, Ab initio molecular dynamics for liquid metals, Phys. Rev. B 47 (1) (1993) 558, https://doi.org/10.1103/PhysRevB.47.558.

[56] P.E. Blöchl, Projector augmented-wave method, Phys. Rev. B 50 (24) (1994) 17953, https://doi.org/10.1103/PhysRevB.50.17953.

[57] S. Grimme, Semiempirical GGA – type density functional constructed with a long-range dispersion correction, J. Comput. Chem. 27 (2006) 1787–1799, https://doi.org/10.1002/jcc.20495.

[58] T.P. Senftle, S. Hong, M.M. Islam, S.B. Kylasa, Y. Zheng, Y.K. Shin, Ch. Junkermeier, R. Engel-Herbert, M.J. Janik, H.M. Aktulga, T. Verstraelen, A. Grama, A.C.T. van Duin, The ReaxFF reactive force-field: development, applications and future directions, npj Comput. Mater. 2 (2016) 15011, https://doi.org/10.1038/npjcompumats.2015.11.

[59] R.T. Cygan, J.J. Liang, A.G. Kalinichev, Molecular models of hydroxide, oxyhydroxide, and clay phases and the development of a general force field, J. Phys. Chem. B 108 (4) (2004) 1255–1266, https://doi.org/10.1021/jp0363287.

[60] Q. Zheng, J. Jiang, G. Xu, J. Yu, L. Tang, S. Li, New insights into the role of portlandite in the cement system: elastic anisotropy, thermal stability, and structural compatibility with C-S-H, Cryst. Growth Des. 20 (2020) 2477–2488, https://doi.org/10.1021/acs.cgd.9b01644.

[61] Consistent Valence Force Field, (CVFF) documentation. www.uoxray.uoregon.edu/local/manuals/biosym/discovery/General/Forcefields/CVFF.html, 2023. (Accessed 4 February 2023).

[62] T.R. Cygan, J.A. Greathouse, A.G. Kalinichev, Advances in clayff molecular simulation of layered and nanoporous materials and their aqueous interfaces, J. Phys. Chem. C 125 (32) (2021) 17573–17589, https://doi.org/10.1021/acs.jpcc.1c04600.

[63] N. Loganathan, B.O. Ferguson, B. Arey, H.E. Argersinger, G.M. Bowers, A mechanistic exploration of natural organic matter aggregation and surface complexation in smectite mesopores, J. Phys. Chem. A 124 (2020) 9832–9843, https://doi.org/10.1021/acs.jpca.0c08244.

[64] J.L. Suter, R.L. Anderson, H.Ch. Greenwell, P.V. Coveney, Recent advances in large-scale atomistic and coarse-grained molecular dynamics simulation of clay minerals, J. Mater. Chem. 19 (2009) 2482–2493, https://doi.org/10.1039/B820445D.

[65] M.A. Mazo, L.I. Manevitch, E.B. Gusarova, M.Y. Shamaev, A.A. Berlin, N. K. Balabaev, G.C. Rutledge, Molecular dynamics simulation of thermomechanical properties of montmorillonite crystal. 3. Montmorillonite crystals with PEO

oligomer intercalates, J. Phys. Chem. B 112 (2008) 3597–3604, https://doi.org/10.1021/jp076028f.
[66] P. Dauber-Osguthorpe, V.A. Roberts, D.J. Osguthorpe, J. Wolff, M. Genest, A. T. Hagler, Structure and energetics of ligand binding to proteins: Escherichia coli dihydrofolate reductase-trimethoprim, a drug-receptor system, Proteins Struct. Funct. Bioinf. 4 (1988) 31–47, https://doi.org/10.1002/prot.340040106.
[67] J.A. Greathouse, R.T. Cygan, J.T. Fredrich, G.R. Jerauld, Adsorption of aqueous crude oil components on the basal surfaces of clay minerals: molecular simulations including salinity and temperature effects, J. Phys. Chem. C 121 (2017) 22773–22786, https://doi.org/10.1021/acs.jpcc.7b06454.
[68] S. Plimpton, Fast parallel algorithms for short-range molecular dynamics, J. Comput. Phys. 117 (1995) 1–19, https://doi.org/10.1006/jcph.1995.1039.
[69] W.G. Hoover, Canonical dynamics: equilibrium phase-space distributions, Phys. Rev. A 31 (1985) 1695, https://doi.org/10.1103/PhysRevA.31.1695.
[70] M. Parrinello, A. Rahman, Crystal structure and pair potentials: a molecular-dynamics study, Phys. Rev. Lett. 45 (1980) 1196–1199, https://doi.org/10.1103/PhysRevLett.45.1196.
[71] J.D. Gale, GULP: a computer program for the symmetry-adapted simulation of solids, J. Chem. Soc. Faraday Trans. 93 (1997) 629–637, https://doi.org/10.1039/A606455H.
[72] R.J. Bell, P. Dean, Atomic vibrations in vitreous silica, Discuss. Faraday Soc. 50 (1970) 55–61, https://doi.org/10.1039/DF9705000055.
[73] D.C. Montgomery, G.C. Runger, Applied Statistics and Probability for Engineers, Wiley & Sons, 1994.
[74] I.G. Richardson, The calcium silicate hydrates, Cem. Concr. Res. 38 (2008) 137–158, https://doi.org/10.1016/j.cemconres.2007.11.005.
[75] I.G. Richardson, Model structures for C-(A)-S-H(I), Acta Crystallogr. B70 (2014) 903–923, https://doi.org/10.1107/S2052520614021982.
[76] M.J.A. Qomi, K.J. Krakowiak, M. Bauchy, K.L. Stewart, R. Shahsavari, D. Jagannathan, D.B. Brommer, A. Baronnet, M.J. Buehler, S. Yip, F.J. Ulm, K. J. Van Vliet, R.J.M. Pellenq, Combinatorial molecular optimization of cement hydrates, Nat. Commun. 5 (2014) 4960, https://doi.org/10.1038/ncomms5960.
[77] J.J. Thomas, H.M. Jennings, A.J. Allen, Relationship between composition and density of tobermorite, jennite and nanoscale $CaO\text{-}SiO_2\text{-}H_2O$, J. Phys. Chem. C 114 (2010) 7594–7601, https://doi.org/10.1021/jp910733x.
[78] M.J.A. Qomi, M. Bauchy, F.J. Ulm, R.J.M. Pellenq, Anomalous composition-dependent dynamics of nanoconfined water in the interlayer of disordered calcium-silicate, J. Chem. Phys. 140 (2014), 054515, https://doi.org/10.1063/1.4864118.
[79] H.M. Jennings, Refinements to colloid model of C-S-H in cement: CM-II, Cem. Concr. Res. 38 (2008) 275–289, https://doi.org/10.1016/j.cemconres.2007.10.006.
[80] M. Ashby, H. Shercliff, D. Cebon, Materials Engineering, Science, Processing and Design, second ed., Butterworth-Heinemann, 2010.
[81] S.N. Hong, C.J. Yu, U.S. Hwang, C.H. Kim, B.H. Ri, Effect of porosity and temperature on thermal conductivity of jennite: a molecular dynamics study, Mater. Chem. Phys. 250 (2020), 123146, https://doi.org/10.1016/j.matchemphys.2020.123146.
[82] S.N. Hong, C.J. Yu, K, K.C. Ri, J.M. Han, B.H. Ri, Molecular dynamics study of the effect of moisture and prosity on the thermal conductivity of tobermortie 14Å, Int. J. Therm. Sci. 159 (2021), 106537 https://doi.org/10.1016/j.ijthermalsci.2020.106537.
[83] D.P. Bentz, Transient plane source measurements of the thermal properties of hydrating cement pastes, Mater. Struct. 40 (2007) 1073–1080, https://doi.org/10.1617/s11527-006-9206-9.
[84] N. Mehra, L. Mu, T. Ji, X. Yang, J. Kong, J. Gu, J. Zhu, Thermal transport in polymeric materials and across composite interfaces, Appl. Mater. Today 12 (2018) 92–130, https://doi.org/10.1016/j.apmt.2018.04.004.
[85] A. Giri, J.P. Niemelä, C.J. Szwejkowski, M. Karppinen, P.E. Hopkins, Reduction in thermal conductivity and tunable heat capacity of inorganic/organic hybrid superlattices, Phys. Rev. B 93 (2016), 024201, https://doi.org/10.1103/PhysRevB.93.024201.
[86] F. Krahl, A. Giri, J.A. Tomko, T. Tynell, P.E. Hopkins, M. Karppinen, Thermal conductivity reduction at inorganic–organic interfaces: from regular superlattices to irregular gradient layer sequences, Adv. Mater. Interfaces 5 (2018) 1701692, https://doi.org/10.1002/admi.201701692.
[87] E.S. Landry, M.I. Hussein, A.J.H. McGaughey, Complex superlattice unit cell designs for reduced thermal conductivity, Phys. Rev. B 77 (2008), 184302, https://doi.org/10.1103/PhysRevB.77.184302.
[88] A. Giri, P.E. Hopkins, J.G. Wessel, J.C. Duda, Kapitza resistance and the thermal conductivity of amorphous superlattices, J. Appl. Phys. 118 (2015), 165303, https://doi.org/10.1063/1.4934511.
[89] T.S. English, J.C. Duda, J.L. Smoyer, D.A. Jordan, P.M. Norris, L.V. Zhigilei, Enhancing and tuning phonon transport at vibrationally mismatched solid-solid interfaces, Phys. Rev. B 85 (2012), 035438, https://doi.org/10.1103/PhysRevB.85.035438.
[90] E.T. Swartz, R.O. Pohl, Thermal boundary resistance, Rev. Mod. Phys. 61 (1989) 605, https://doi.org/10.1103/RevModPhys.61.605.
[91] H. Mizuno, S. Mossa, J.L. Barrat, Beating the amorphous limit in thermal conductivity by superlattices design, Sci. Rep. 5 (2015) 14116, https://doi.org/10.1038/srep14116.
[92] S. Majumdar, J.A. Sierra-Suarez, S.N. Schiffres, W.L. Ong, C.F. Higgs III, A.J. H. McGaughey, J.A. Malen, Vibrational mismatch of metal leads controls thermal conductance of self-assembled monolayer junctions, Nano Lett. 15 (5) (2015) 2985–2991, https://doi.org/10.1021/nl504844d.
[93] H.R. Seyf, A. Henry, A method for distinguishing between propagons, diffusions, and locons, J. Appl. Phys. 120 (2016), 025101, https://doi.org/10.1063/1.4955420.
[94] W.X. Zhou, Y. Cheng, K.Q. Chen, G. Xie, T. Wang, G. Zhang, Thermal conductivity of amorphous materials, Adv. Funct. Mater. 30 (2020) 1903829, https://doi.org/10.1002/adfm.201903829.
[95] I.G. Richardson, Tobermorite/jennite- and tobermorite/calcium hydroxide-based models for the structure of C-S-H: applicability to hardened pastes of tricalcium silicate, β-dicalcium silicate, Portland cement, and blends of Portland cement with blast-furnace slag, metakaolin, or silica fume, Cem. Concr. Res. 34 (2004) 1733–1777, https://doi.org/10.1016/j.cemconres.2004.05.034.
[96] R.J.M. Pellenq, A. Kushima, R. Shahsavari, K.J. Van Vliet, M.J. Buehler, S. Yip, F. J. Ulm, A realistic molecular model of cement hydrates, PNAS. 106 (2009) 16102–16107, https://doi.org/10.1073/pnas.0902180106.
[97] S. Grangeon, F. Claret, Y. Linard, C. Chiaberge, X-ray diffraction: a powerful tool to probe and understand the structure of nanocrystalline calcium silicate hydrates, Acta Crystallogr. Sect. B: Struct. Sci. Cryst. Eng. Mater. B69 (2013) 465–473, https://doi.org/10.1107/S2052519213021155.
[98] D.G. Cahill, R.O. Pohl, Heat flow and lattice vibrations in glasses, Solid State Commun. 70 (1989) 927–930, https://doi.org/10.1016/0038-1098(89)90630-3.
[99] R. Shahsavari, Hierarchical Modeling of Structure and Mechanics of Cement Hydrate (Ph.D Thesis), Massachusetts Institute of Technology, 2011.
[100] D.A. Kulik, G.D. Miron, B. Lothenbach, A structurally-consistent CASH+ sublattice solid solution model for fully hydrated C-S-H phases: thermodynamic basis, methods, and $Ca\text{-}Si\text{-}H_2O$ core sub-model, Cem. Concr. Res. 151 (2022), 106585, https://doi.org/10.1016/j.cemconres.2021.106585.
[101] G. Geng, R. Nikolayevich Vasin, J. Li, M.J.A. Qomi, J. Yan, H.R. Wenk, P.J. M. Monteiro, Preferred orientation of calcium aluminosilicate hydrate induced by confined compression, Cem. Concr. Res. 113 (2018) 186–196, https://doi.org/10.1016/j.cemconres.2018.09.002.
[102] M. Balonis, F.R. Glasser, The density of cement phases, Cem. Concr. Res. 39 (2009) 733–739, https://doi.org/10.1016/j.cemconres.2009.06.005.
[103] F. Avet, E. Boehm-Courjault, K. Scrivener, Investigation of C-A-S-H composition, morphology and density in Limestone Calcined Clay Cement (LC^3), Cem. Concr. Res. 115 (2019) 70–79, https://doi.org/10.1016/j.cemconres.2018.10.011.
[104] A.K. Mohamed, P. Moutzouri, P. Berruyer, B.J. Walder, J. Siramanont, M. Harris, M. Negroni, S.C. Galmarini, S.C. Parker, K.L. Scrivener, L. Emsley, P. Bowen, The atomic-level structure of cementitious calcium aluminate silicate hydrate, J. Am. Chem. Soc. 142 (2020) 11060–11071, https://doi.org/10.1021/jacs.0c02988.
[105] G. Geng, R. Myers, J. Li, R. Maboudian, C. Carraro, D.A. Shapiro, P.J.M. Monteiro, Aluminum-induced dreierketten chain cross-links increase the mechanical properties of nanocrystalline calcium aluminosilicate hydrate, Sci. Rep. 7 (2017) 44032, https://doi.org/10.1038/srep44032.
[106] J. Langford, A. Wilson, Scherrer after sixty years: a survey and some new results in the determination of crystallite size, J. Appl. Crystallogr. 11 (1987) 102–113, https://doi.org/10.1107/S0021889878012844.
[107] P. Scherrer, Bestimmung der grosse und der inneren struktur von kolloidteilchen mittels rontgenstrahlen, Nachr. Ges. Wiss. Gottingen 26 (1918) 98–100.
[108] G. Latini, G. Passerini, Silanes and siloxanes thermal conductivity in the liquid phase: a critical review and an improved prediction method, Tec. Ital. 65 (2021) 212–217, https://doi.org/10.18280/ti-ijes.652-411.
[109] R.C. Hill, W.E. Griffiths, G.C. Lim, Principles of Econometrics, fourth ed., Willey, 2011.